A time domain procedure for the identification of periodic structures

A time domain procedure for the identification of periodic structures

Fabrizio Aloschi*[a,b], Oreste Salvatore Bursi[a], Antonio Palermo[c], Alessandro Marzani[c]

[a] *Department of Civil, Environmental and Mechanical Engineering (DICAM), University of Trento, Italy*
[b] *Department of Structures for Engineering and Architecture (DIST), University of Naples Federico II, Italy*
[c] *Department of Civil, Chemical, Environmental, and Materials Engineering (DICAM), University of Bologna, Italy*

Abstract

A procedure for the identification of dispersion curves and mechanical characteristics of linear and nonlinear one-dimensional (1D) periodic structures is proposed herein. The procedure exploits the application of Floquet–Bloch (F–B) boundary conditions to a reference subsystem (RS) extracted from a mechanical metastructure. The dispersion curves (frequency vs. wavenumbers) are estimated from the computation of the frequency response functions (FRFs) of the RS for different wavenumbers in input. The proposed procedure is applied and validated on various models, including a 1D mass-in-mass system characterized by cubic nonlinear springs. As expected, the nonlinear system exhibits a distinct dependence on the amplitude of the excitation. In addition, a revised application of the subspace identification (SI) method is exploited for the identification of hardening-type nonlinear mechanical characteristics. For the sake of completeness, the identification procedure is also tested on a waveguide in axial and flexural vibrations. Due to its single output from a measuring cell, and two inputs, the proposed method is particularly suitable for the experimental characterization of periodic structures.

Keywords: Discrete periodic nonlinear systems, Euler–Bernoulli beam, Dispersion curve identification, Floquet–Bloch theory application, Subspace identification.

1. Introduction

1.1. Background and motivation

Recent years have witnessed a growing interest in the peculiar characteristics of mechanical metamaterials and periodic structures. Amidst an incredibly vast array of applications, spanning from lightweight structures [1, 2, 3], hierarchical lattices [4, 5], to dissipative systems [6, 7] and even mechanical computers [8, 9], they have also been proposed to mitigate the effects of low-frequency vibrations [10, 11, 12]. Periodic structures support the propagation of waves with strong dispersive features that are not solely determined by wave speeds or wavenumbers. They arise due to material

*Corresponding author: fabrizio.aloschi@unina.it, fabrizioaloschi@gmail.com

properties and structural design [13, 14, 15, 16]. Specifically, frequency bandgaps can arise either from Bragg scattering [17, 18] or from the interaction of incident waves with a periodic arrangement of locally resonant elements [17, 19, 20]. In both scenarios, this interaction leads to the blocking of waves characterized by specific frequency ranges [21, 22, 23]. However, in the latter case, which we refer to as *mass-in-mass* systems, the bandgaps form for wavelengths higher than the lattice dimensions [24]. Along these lines, the identification of such media for crack detection and damage quantification has become essential [25, 26, 27] and relies on the analysis of dispersion curves that, for linear systems, establish a one-to-one correspondence between frequencies and wavenumbers.

This correspondence vanishes in the context of nonlinear mechanical metamaterials, wherein the nonlinearity causes physical phenomena such as higher harmonics and amplitude-dependent dispersion relationships [28]. Concerning analysis methods, we have to distinguish between weakly and strongly nonlinear systems [29]. Since we are interested in weakly nonlinear systems, we recall multiple scales, Lidstedt-Poincaré and perturbation techniques applied to elastic metamaterials [30]. The harmonic balance method [31], instead, has been applied to strongly nonlinear periodic systems. To improve the performance of metamaterial-based systems, nonlinear mechanisms were adopted. For instance, one can look at the research works that use the concept of quasi-zero or negative stiffness [32], proposed in [33, 34, 35]; they showed that quasi-zero or negative stiffness resonant elements could improve the system behaviour and reduce resonator sizes. Also, bistable metamaterials have been used to control mechanical waves. In this respect, it is deemed necessary to mention: i) Xia et al. [36], who enhanced the bandwidth of nonlinear metastructures by means of bistable nonlinearities in the resonators; ii) Deng et al. [37], who analyzed the behavior of waves in free-standing bistable discrete periodic systems; iii) Guner et al., 2023, [38] who employed bistable columns to increase the dissipation properties of coupled metafoundation-tank systems against seismic vibrations.

The characterization of the aforementioned nonlinear periodic systems typically requires the determination of the amplitude-dependence or the wavenumber dependence. Hence, for characterizing nonlinear waves [39], the dispersion is assumed to rise linearly and is subsequently complemented with nonlinear terms. For instance, to study wave-wave interactions, Manktelow et al. [40] introduced nonlinear dispersion relations to define curves that were *corrected*, w.r.t. their linear counterparts. Similarly, Campana et al. [41] identified correction terms to account for the presence of nonlinear resonators. In the remainder of this paper, though the uniqueness of dispersion curves is lost in a nonlinear setting, we will refer to these curves as *nonlinear dispersion curves*. Disper-

sion curves of both linear and nonlinear structures are commonly computed through i) numerical responses of finite lattices, ii) experimental outputs, and iii) analytical tools.

With respect to i), several methods employ the integration of the equations of motion (EoM) of sufficiently long finite chains, eventually employing absorbing boundaries to avoid wave reflection. Fang et al. [42] compared the results of numerical simulations with predictions obtained from the harmonic averaging approach and Lyapunov exponents. Additionally, they performed a linearized estimation obtained by applying the Floquet–Bloch (F–B) theorem. The F–B theorem is a widely employed tool for computing dispersion curves in periodic 1D, 2D, and 3D systems [43, 44]. It was also used by Settimi et al. [45], Wang et al. [46], Sepehri et al. [47] and Campana et al. [41], in the context of nonlinear systems; they similarly computed the nonlinear dispersion curves of periodic structures using a perturbation approach.

Regarding ii), numerous methods are devoted to the identification of wave vectors and dispersion curves from experimental responses [48, 49, 50, 51]. Junyi et al. [48] developed an inverse method to calculate the band structure of 1D periodic structures. The method is called wave superposition method (WSM), because it employs the superposition of forward and back waves coming from periodic oscillations. The proposed method is validated with numerical experiments on a periodic bi-material beam modeled with the Timoshenko beam theory. The WSM is particularly useful when a model of the physical structure is unavailable, but the method is accurate under ideal conditions, hence experimental aspects of the WSM were deferred to future studies [52]. The WSM eliminates the need for a structural model through the use of multiple measurements, constituting a data-driven approach. Other data-driven methods for reconstructing dispersion curves exist [53, 54], validated through successful numerical experiments. However, data-driven methods may face limitations in scalability across frequency and spatial dimensions due to their reliance on multiple measurements. Additionally, they may require substantial computational resources for accommodating real data from large structures. In our study, we address these issues by means of a reference subsystem (RS) consisting of a single cell of the structure. The RS, excited with F–B boundary conditions, preserves all essential information about the periodic structure while significantly reducing computational demand.

With regard to iii), a number of approximate analytical methods have been devoted to the prediction of nonlinear dispersion curves. Among others, we recall those based on the harmonic balance

[55, 56], the perturbation method [45, 46, 57], the homotopy harmonic balance [58], the homotopy Padé technique [59], the multiple scales [60], and the factorization of the spatial and temporal parts of the solution [61]. Analytical methods are advantageous because they provide closed-form solutions that can be easily compared with numerical predictions in the validity range of linearization. In this paper, we propose a perturbation approach to approximate the nonlinear FRF and validate the identified dispersion curve. For the sake of comparison, we leverage the solution proposed by Zivieri et al. [61].

1.2. Scope

We propose a methodology based on the FRF of an RS to define dispersion laws and mechanical characteristics of periodic structures. The RS is extracted from a periodic mechanical metastructure and represents the prototype of an experimentally informed model. In this respect, the F–B periodic conditions are applied to the boundaries of the RS. Following a standard approach, we initially discuss the system identification strategy for discrete mass-in-mass systems. Then, we extend the approach to one-dimensional waveguides. Additionally, since the identification of discrete mass-in-mass systems in a pure analytical/numerical setting is quite simple, we leverage the generality of the FRF and F–B tools and treat weakly nonlinear periodic systems. Finally, to bridge the gap between the proposed numerical framework and future experimental activities, we incorporate noise in the numerical examples and apply the subspace identification (SI) technique.

The remainder of this paper is organized as follows. In Section 2, we introduce the general problem including the RS, and elucidate the main identification procedure for the dispersion curves. Section 3 reports the identification of the nonlinear dispersion curves of a nonlinear mass-in-mass metamaterial. The SI is introduced and applied for the identification of both the linear and nonlinear stiffness constants. A brief discussion on the identification of a mass-in-mass system with nonlinear resonators concludes Section 3. Section 4 reports a simplified methodology to identify the dispersion curves of a linear undamped mass-in-mass system. Then, in Section 5 an application of the dispersion curve identification procedure to a continuous beam in axial and flexural vibrations is shown. We draw conclusions in Section 6 with possible future directions. Finally, Appendix A provides supplementary material for the perturbation approach introduced in Section 3 while Appendix B describes the implementation details for the transfer matrix method relevant to Section 5. A MATLAB code example that solves the numerical procedure described in Section 2 is provided as Supplementary Material.

2. Dispersion curves identification strategy

For the sake of generality, this section introduces the basic concept behind the identification procedure using a nonlinear discrete one-dimensional (1D) periodic structure. Notably, as demonstrated later, the same strategy applies to both discrete and continuous linear systems.

The discrete mass-in-mass structure consists of units with external masses encasing resonating masses, connected by means of viscous dampers and internal springs, as shown in Fig. 1 (a).

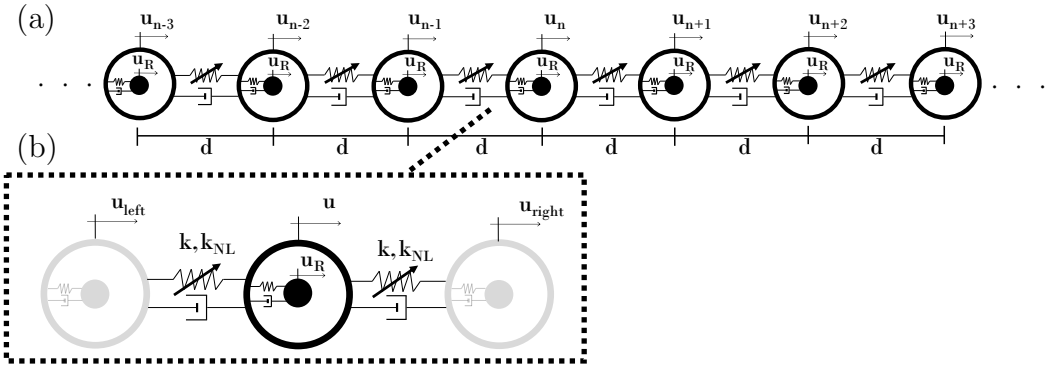

Figure 1: (a) 1D discrete mass-in-mass metamaterial modeled with nonlinear springs and dashpots, and (b) the relevant reference subsystem (RS).

The reference subsystem (RS) is depicted in Fig. 1 (b). To take into account nonlinearities, the elastic internal force F between two adjacent external masses is assumed as follows:

$$F(\delta_i) = k\,\delta_i + k_{NL}\delta_i^3, \tag{1}$$

where both a linear k and nonlinear k_{NL} springs are considered, and where $\delta_i = u_{n\pm1} - u_n$ denotes the relative displacement between the two masses. The u_n displacement of the n^{th} unit can be generally written as [21]:

$$u_n(t) = U(\kappa,\omega)\,\exp\big[i(n\kappa d + \omega t)\big], \tag{2}$$

where ω is the circular frequency of the harmonic motion, κ is the complex wavenumber, U is the wave motion amplitude, d represents the distance between the periodic units, and i is the imaginary number. The exponential term defines the periodicity in space and time, as $|\exp\big[i(n\kappa d + \omega t)\big]| \leq 1$ [62]. The real part of the wavenumber describes the phase change as the wave propagates from one unit to the next, whereas its imaginary part defines the amplitude decay of the wave. To replicate the infinite chain's dynamics using the RS, we impose the F–B boundary conditions on its left- and right-hand bounds, namely, $u_{n-1} = u_{left}$ and $u_{n+1} = u_{right}$, as shown in Fig. 1 (b), and monitor the displacement output of the reference unit $u_n = u$. The identification of the dispersion curves is

based on the FRF of the RSs excited by imposed displacements of the F–B type. According to (2), the output displacement $u(t)$ should fulfill the following conditions:

$$u(t) = u_{left}(t)\exp(i\kappa d) = u_{right}(t)\exp(-i\kappa d), \tag{3}$$

From (3), we derive a system of equations:

$$\begin{cases} FRF_{left} = \dfrac{U}{U_{left}} = \exp(i\kappa_r d)\exp(-\kappa_i d), \\ \\ FRF_{right} = \dfrac{U}{U_{right}} = \exp(-i\kappa_r d)\exp(\kappa_i d), \end{cases} \tag{4}$$

where κ_r and κ_i are the real and imaginary part of the wavenumber, respectively; U_{left} and U_{right} are the amplitudes of the displacements imposed on the left and right boundaries of the RS that satisfy (2). Consequently, the transmission ratios of (4) describe the output of a 1D infinite periodic chain. By means of (4), we derive the following system:

$$\begin{cases} f_1(\kappa_r, \kappa_i) = \Phi_{left} - \exp(i\kappa_r d)\exp(-\kappa_i d), \\ f_2(\kappa, \kappa_i) = \Phi_{right} - \exp(-i\kappa_r d)\exp(\kappa_i d), \end{cases} \tag{5}$$

where Φ is the numerical FRF computed as the ratio between the Fourier transform (FT) of the output and input, the subscripts $left$ and $right$ refer to the input and d defines the distance between the unit cells. From (5), we formulate the corresponding model function $F(\kappa)$ as follows:

$$F(\kappa) = \begin{bmatrix} f_1(\kappa_r, \kappa_i) \\ f_2(\kappa_r, \kappa_i) \end{bmatrix}, \tag{6}$$

that is nonlinear in the complex model parameter κ. The solution to (5) is obtained by optimizing κ in (6) in the context of a nonlinear least squares problem, which we address using the Levenberg–Marquardt algorithm [63, 64]. This optimization algorithm minimizes $F(\kappa)$ by employing a search direction that can be viewed as a blend of the Gauss–Newton direction and the Cauchy steepest descent. Its convenience is notable because the Jacobian is consistently characterized by full rank at each iteration. However, for its convergence, it is essential that the residuals evaluated in the first step are not excessively high [64]. A pseudo-code for the identification procedure, which incorporates this minimization process, is provided in Fig. 2.

begin

input: ω, U_{left}, first guess ($\kappa_{r,0}$, $\kappa_{i,0}$), max num of iter (N), tolerance (tol)

for $\omega = 0$ to the maximum frequency of interest

n$\leftarrow$1

while (n $\leqslant$ N)

$\Phi_{left} \leftarrow \dfrac{FT\left[u(\kappa_{r,n-1},\, \kappa_{i,n-1})\right]}{FT\left(u_{left}\right)}$

$\Phi_{right} \leftarrow \dfrac{FT\left[u(\kappa_{r,n-1},\, \kappa_{i,n-1})\right]}{FT\left(u_{right}\right)}$

> ***if*** (n = N)
>
> j$\leftarrow$1
>
> $\kappa_{i,j-1} = \kappa_{i,n}$
>
> > ***while*** (j $\leqslant$ N)
> >
> > $|\Phi_{left}| \leftarrow \left|\dfrac{FT\left[u(\kappa_{r,N},\, \kappa_{i,j-1})\right]}{FT\left(u_{left}\right)}\right|$
> >
> > ***if*** $\left(\|\nabla f_1(\kappa_{r,N}, \kappa_{i,j})\|_\infty\right) \leqslant tol$
> >
> > m$\leftarrow$1
> >
> > $\kappa_{r,m-1} = \kappa_{r,N}$
> >
> > > ***while*** (m $\leqslant$ N)
> > >
> > > $\Phi_{left} \leftarrow \dfrac{FT\left[u(\kappa_{r,m-1},\, \kappa_{i,j})\right]}{FT\left(u_{left}\right)}$
> > >
> > > ***if*** $\left(\|\nabla f_1(\kappa_{r,m}, \kappa_{i,j})\|_\infty\right) \leqslant tol$
> > >
> > > ***break***
> > >
> > > ***end if***
> > >
> > > ***end while***
> >
> > ***end if***
> >
> > ***end while***
>
> ***end if***

if $\left(\|\nabla f_1(\kappa_{r,n}, \kappa_{i,n})\|_\infty \;\&\; \|\nabla f_2(\kappa_{r,n}, \kappa_{i,n})\|_\infty\right) \leqslant tol$

break

end if

end while

end for

Figure 2: Pseudo-code for the identification of dispersion curves.

More precisely, for the selected ω, at each iteration n the RS is excited for free-wave solutions with input parameters $\kappa_{r,n}, \kappa_{i,n}$. The output $FT[u]$ is estimated, and rows 5 and 6 are computed. If the least-squares problem (6) is not solved after $n = N$ iterations, that is, if row 24 is not satisfied for $(\kappa_{r,N}, \kappa_{i,N})$, the last solution $\kappa_{r,N}$ is imposed as known solution in an additional least-squares problem (row 10), where only the first of the equations in (5) is employed in the unknown $\kappa_{i,j}$. Then, the while loop in row 15, with the last solution $\kappa_{i,j}$ and initial condition $\kappa_{r,N}$ for the unknown $\kappa_{r,m}$, completes the identification process. The initial guess $\kappa_{r,0}$ is arbitrary due to the periodic nature of $\exp(\pm i\kappa_r d)$. Conversely, to prevent convergence issues, $\kappa_{i,0}$ should be kept relatively low. It is advisable to initiate with a very-low value for $\kappa_{i,0}$ and increment it if convergence is not achieved. Nevertheless, the order of magnitude of $\kappa_{i,0}$ can be easily guessed, as users generally know whether the system is within the bandgap or the passband.

In sum, we can identify the dispersion curves of infinite 1D periodic systems with unknown parameters using the simple RS and the procedure sketched in Fig. 2. As shown later in Section 4, this process can be further simplified when a discrete linear undamped system is identified. A MATLAB routine implementing the procedure described in Fig. 2 for the mechanical system depicted in Fig. 1 is provided as Supplementary Material.

3. Nonlinear mass-in-mass system: identification of nonlinear dispersion curves and relevant nonlinear mechanical parameters

To capture the dispersion's dependency on the excitation amplitude [65], researchers have frequently applied the Floquet–Bloch (F–B) theorem to linearized systems [41, 42, 66]. However, when the cubic nonlinearity in (1) is significant, the application of the F–B conditions may become inaccurate, as it will be shown in Section 3.1. Moreover, to simulate a real-world experimental setting, noise is introduced into time histories in Section 3.2, and treated using the subspace identification (SI). Finally, Subsection 3.3 extends the identification approach to a mechanical metamaterial equipped with nonlinear resonators.

3.1. Nonlinear dispersion curves identification

In this subsection, we describe the application of the proposed identification procedure to a nonlinear mass-in-mass system characterized by the restoring force expressed by (1). The nonlinearity is of the cubic-hardening type, and the relevant reference subsystem (RS) is depicted in Fig. 3.

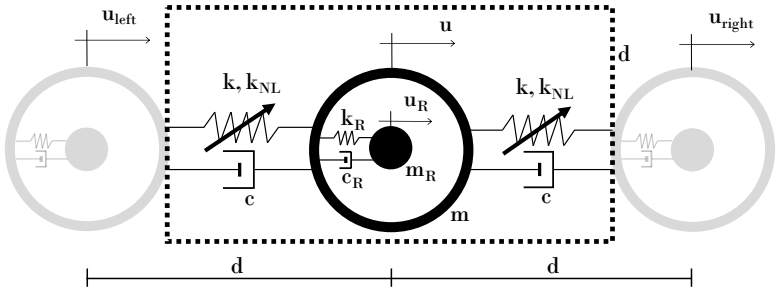

Figure 3: Reference subsystem (RS) for the 1D nonlinear mass-in-mass metamaterial.

The system of EoMs reads:

$$\begin{cases} m\ddot{u} + c\big(2\dot{u} - v_{left} - v_{right}\big) + k\big(2u - u_{left} - u_{right}\big) + c_R\big(\dot{u} - \dot{u}_R\big) \\ +k_R\big(u - u_R\big) + k_{NL}(u - u_{left})^3 + k_{NL}(u - u_{right})^3 = 0, \\ m_R\ddot{u}_R + c_R\big(\dot{u}_R - \dot{u}\big) + k_R\big(u_R - u\big) = 0, \end{cases} \tag{7}$$

where k_{NL} denotes the nonlinear spring constant. Based on the F–B boundary conditions, the imposed displacements u_{left} and u_{right} are selected as follows:

$$u_{left} = U_{left}\exp(i\omega t), \tag{8}$$

$$u_{right} = u_{left}\exp(2i\kappa d), \tag{9}$$

where U_{left} is the amplitude of the imposed motion and κ and ω are the input wavenumber and circular frequency, respectively; d is the distance between the unit cells. To identify the dispersion curves, we implement the identification procedure reported in Fig. (2).

The mechanical properties of the RS are shown in Fig. 3: $m = 2450\,\mathrm{kg}$, $k = 155\,\mathrm{kN/m}$, $m_R = 3170\,\mathrm{kg}$, $k_R = 1080\,\mathrm{kN/m}$, $k_{NL} = 200\,\mathrm{MN/m^3}$, $d = 1\,\mathrm{m}$. These values describe a nonlinear mechanical system similar to the one investigated by Zivieri et al. [61]. Damping will be introduced later. For this undamped case, we compare the numerical results with the approximate nonlinear dispersion relation proposed by Zivieri et al. [61] for real wavenumbers:

$$\begin{aligned} mm_R\omega^4 - \big[k_R(m + m_R) + 2m_Rk\big(1 - \cos(\kappa d)\big) + 2m_RU^2k_{NL}\,G(\kappa d)\big]\omega^2 \\ +2k_R\big[k\big(1 - \cos(\kappa d)\big) + k_{NL}U^2G(\kappa d)\big] = 0, \end{aligned} \tag{10}$$

where $G(\kappa d) = \frac{1}{3!}[1 - \cos(3\kappa d) + 3\cos(2\kappa d) - 3\cos(\kappa d)]$ is a wavenumber-dependent series, U defines the amplitude and the distance d between the masses is equal to 1. A comparison between the

identified and approximate solutions is presented in Figs. 4 and 5, where an amplitude of U = 10 and U = 15 mm have been considered, respectively. These amplitudes can be regarded as weak nonlinearities associated to weak anharmonic energies [61].

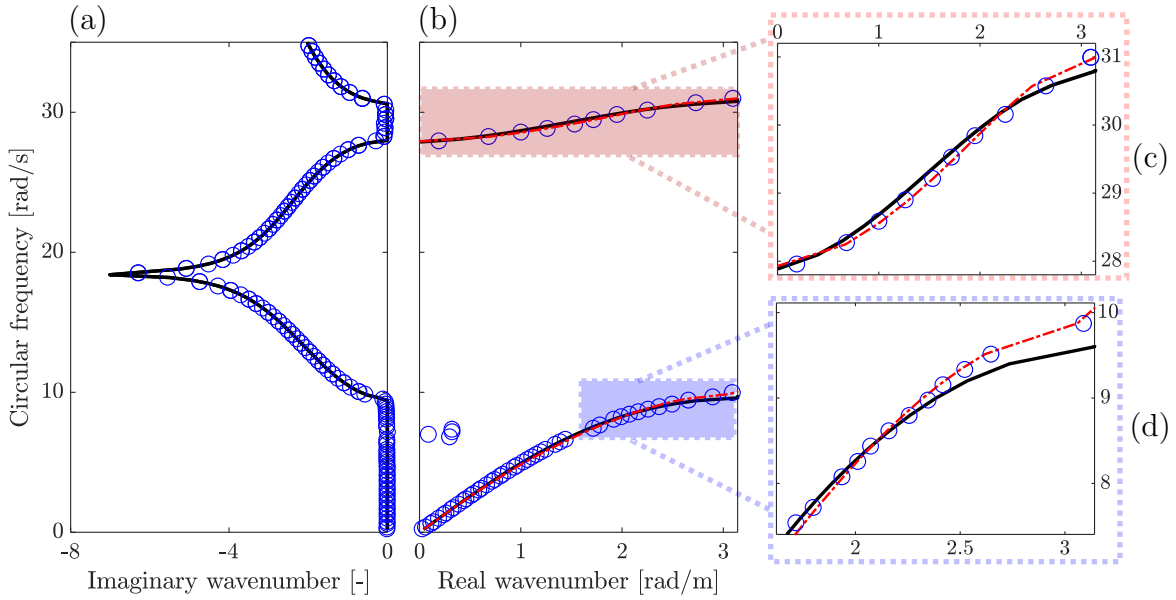

Figure 4: Identification of the nonlinear undamped periodic system for amplitude U = 10 mm: (a) plot of the imaginary components κ_i and (b) real components κ_r of the wavenumber. Close-up of (c) the optical branch and (d) the acoustic branch. The black curve defines the linear solution, the red curve depicts the *nonlinear dispersion curve* from Eq. (10), and the blue circles represent the ID solutions.

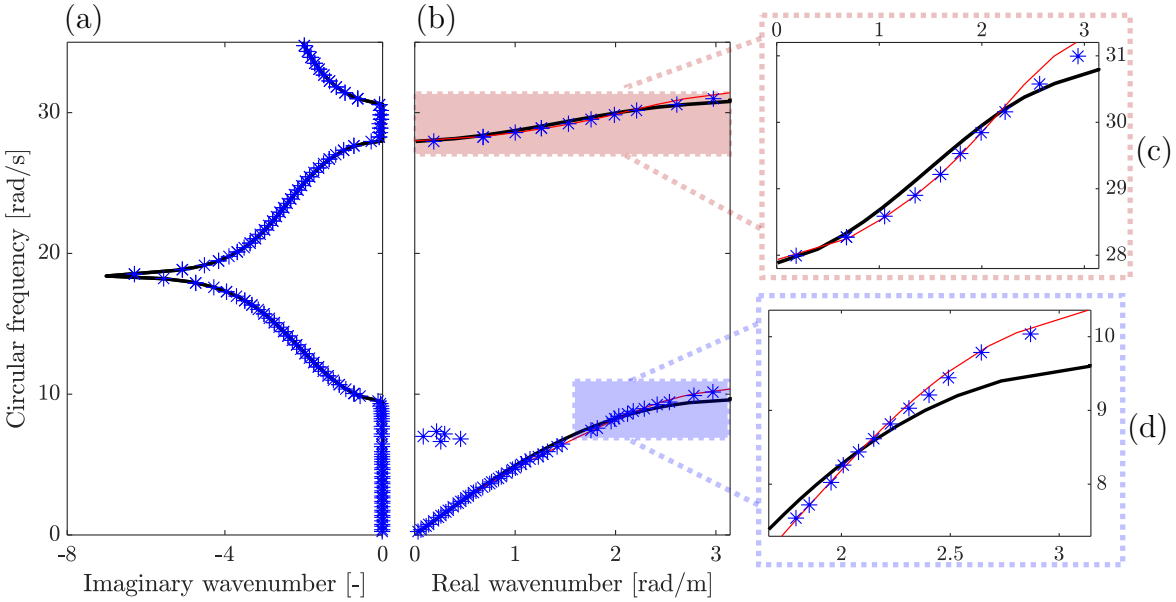

Figure 5: Identification of the nonlinear undamped periodic system for amplitude U = 15 mm: (a) plot of the imaginary components κ_i and (b) real components κ_r of the wavenumber. Close-up of (c) the optical branch and (d) the acoustic branch. The black curve depicts the linear solution, the red curve defines the *nonlinear dispersion curve* from Eq. (10), and the blue markers represent the ID solutions.

Both Fig. 4 and 5 show that the identification process has not been impaired by the initial guesses; however, some outliers appear in the first passband due to failures in the integration of (5) around the first natural frequency of the unit cell of the RS. Furthermore, we recognize that the dependence

of the dispersion curves on the amplitude is not evident neither in Fig. 4 (b) nor in Fig. 5 (b), and the nonlinear solutions seem to be pairing the linear ones. To better highlight the dependency of the dispersive properties on the input amplitude, we zoomed in Figs. 4 (c) and (d), and in Figs. 5 (c) and (d), the identified optical and acoustic branches against the linear ones. In those frequency ranges, a tenuous deviation from the linear curves can be observed, according to the approximate solution of Zivieri et al. [61], i.e., Eq. (10).

We further corroborate the results through simulations on a finite lattice constituted by 50 unit cells and perfectly-matched layers (PMLs) to avoid wave reflections. The lattice is excited with a Ricker wavelet of amplitude U_l and central frequency $\omega_l = 25$ [rad/s]. The time histories' 2D FFT and the amount of restoring force for each level of nonlinearity are reported in Fig. 6.

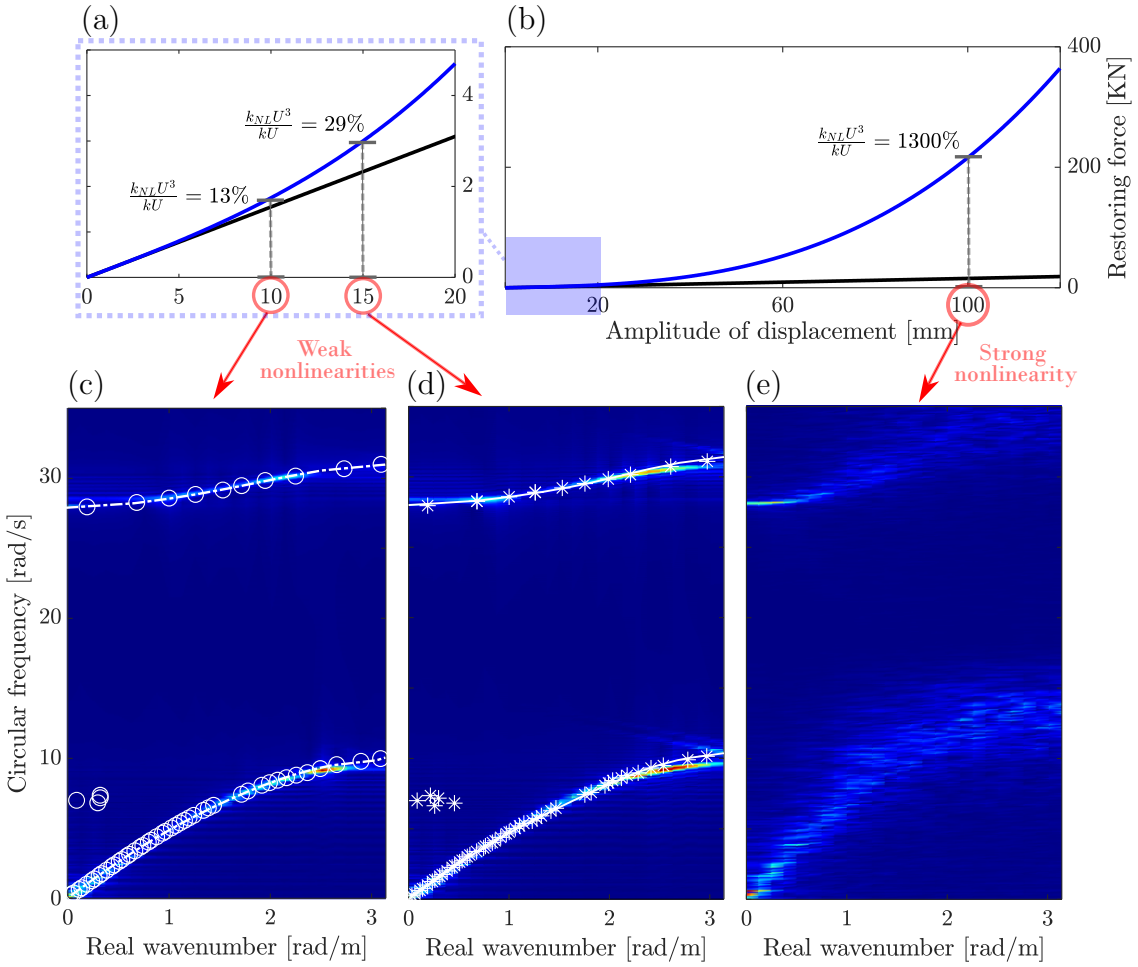

Figure 6: Restoring force-displacement diagram in the range of (a) weak nonlinearity and (b) strong nonlinearity. Finite lattice dispersion curves from the 2D-FFT for two weakly nonlinear cases, (c) U = 10 mm and (d) U = 15 mm, and for a strongly nonlinear case (e) U = 100 mm. (a), (b) The blue curve depicts the nonlinear restoring force $F(U) = kU + k_{NL}U^3$ and the black curve defines the linear force $F(U) = kU$. The circles and stars in (c) and (d) represent the identification results already reported in Figs. 4 and 5, respectively, while the continuous curves depict the approximate solutions from (10).

By using simulations, it is possible to highlight different aspects of the identification problem being

treated. Notably, when dealing with weak nonlinearities, there are minimal deviations in the nonlinear dispersion curves with respect to the linear case. On the other hand, for strong nonlinearities, a distinct hardening effect emerges and the dispersion curve exhibits a diffusion, due to additional frequency components and wave mode couplings [39, 67]. Beyond this amplitude, periodic solutions are no longer found.

To further corroborate the results of the proposed procedure, we compared the numerical values of the transmission function Φ_{left} with an analytical expression of the FRF. For this purpose, we consider a harmonic solution for the displacements u and u_R in (7), and before linearization, we apply the F–B theorem. We obtain the following expression for the nonlinear transmission:

$$\frac{U}{U_{left}} = \frac{k\,(1+e^{2i\kappa d})}{-m\omega^2+2k+k_R-\frac{k_R^2}{k_R-\omega^2 m_R}} - \frac{K(e^{ji\kappa d})\;k_{NL}\,e^{2i\omega t}}{U_{left}\big(-m\omega^2+2k+k_R-\frac{k_R^2}{k_R-\omega^2 m_R}\big)}, \tag{11}$$

where i is the imaginary unit, and the function $K(e^{ji\kappa d})$ comprises higher orders j of the wavenumber,

$$\begin{aligned} K(e^{ji\kappa d}) = &- U_{left}^3 + 3UU_{left}^2 e^{i\kappa d} - 3U^2 U_{left} e^{2i\kappa d} + 2U^3 e^{3i\kappa d} - \\ &3U^2 U_{left} e^{4i\kappa d} + 3UU_{left}^2 e^{5i\kappa d} - U_{left}^3 e^{6i\kappa d}. \end{aligned} \tag{12}$$

The relationship (11) indicates that for a given frequency, the output of the RS depends on the wavenumbers $j\kappa$, with $j \geq 2$, which are naturally associated with superharmonics. Similarly, the dependence on the input amplitude U_{left} is evident. Because the identification procedure proposed in this work relies on (4), this entails that a single complex wavenumber is associated with a given frequency; hence, (4) ignores the components associated with higher-order wavenumbers $j\kappa$.

To further understand the effects of the aforementioned approximation, we utilize a perturbation approach, based on the Lindstedt–Poincaré technique. Based on the asymptotic expansion reported in Appendix A, we obtain:

$$FRF_p = FRF^{(0)} + \epsilon\, FRF^{(1)} + O\,(\epsilon^2), \tag{13}$$

where $FRF^{(0)}$ and $FRF^{(1)}$ read,

$$FRF^{(0)} = \frac{k\left(1+e^{2i\kappa d}\right)}{-m\omega_{(0)}^2 + 2k + k_R - \frac{k_R^2}{k_R - m_R\omega_{(0)}^2}},$$

$$FRF^{(1)} = \left(\frac{8\, m_R\, \omega_{(0)}\, \omega_{(1)} \left({k_R}^2\, m_R + m\, {k_R}^2 - 2\, m\, k_R\, m_R\, \omega_{(0)}^2 + m\, {m_R}^2\, \omega_{(0)}^4\right)}{3\, k_{NL}\, m \left(k_R - m_R\, \omega_{(0)}^2\right)^2 \left(1 - e^{2i\kappa d}\right)^2 |U_{left}|^2}\right)^{\frac{1}{2}}. \tag{14}$$

The order ϵ^0 equation defines the FRF of the linear system and equates the first term on the right-hand side of (11). The expansion of Eq. (13) is arrested at order-ϵ^1, and the relevant order-ϵ^1 equation is an expression that does not depend on the linear stiffness k. It also contains high wavenumbers associated with the frequency $\omega = \omega_{(0)} + \epsilon\,\omega_{(1)}$, which was stopped at the first ϵ^1 order. A comparison between the aforementioned FRF and the transmission obtained as the outcome of the identification procedure based on (4) is shown herein and indicates that the involved approximation is favorable. More precisely, the numerical values of Φ_{left} that satisfy the tolerance of the identification procedure described in the pseudocode in Fig. 2 are plotted in Fig. 7; they correspond to the set of solutions already presented in Fig. 4, for $U_{left} = 10$ mm.

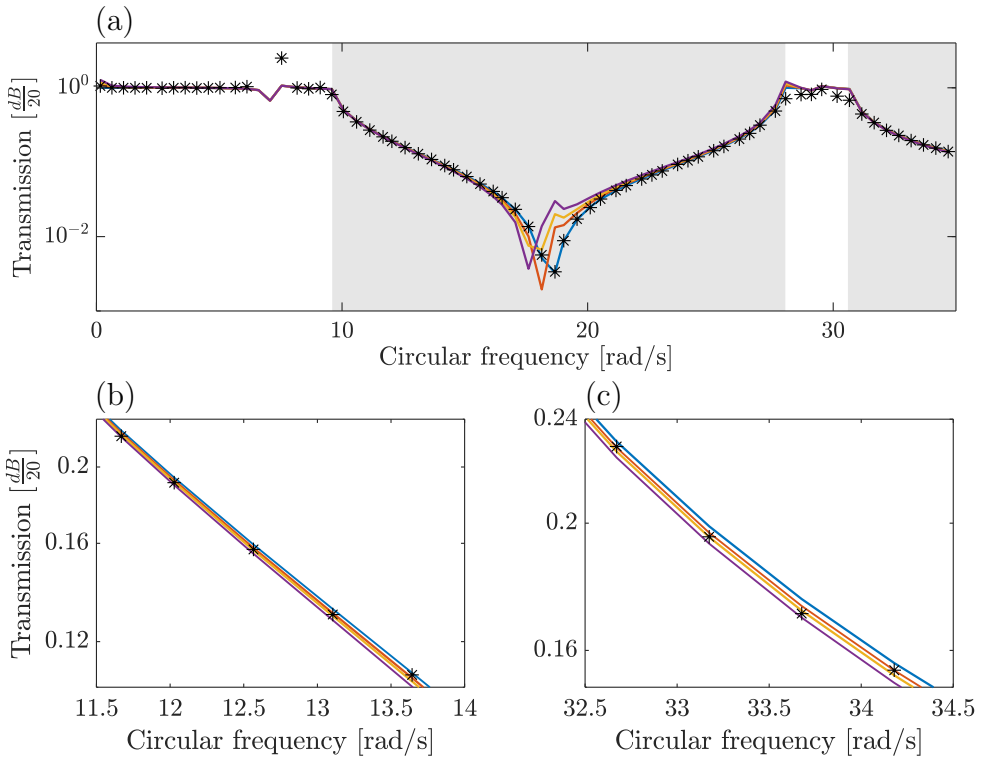

Figure 7: Comparison between the numerical transmission and the analytical $|FRF_p|$ of Eq. (13): (a) the gray areas highlight the bandgaps, (b) a close-up on the range of frequencies in the first bandgap and, (c) in the second bandgap. The blue curve defines the linear $|FRF^{(0)}|$, while the orange, yellow, and violet curves depict the $|FRF_p|$ for $\epsilon = 3 \cdot 10^{-4}$, $\epsilon = 5 \cdot 10^{-4}$, and $\epsilon = 8 \cdot 10^{-4}$, respectively. The black markers represent the numerical values of $|\Phi_{left}|$.

Fig. 7 (a) clearly shows that the numerical values of Φ_{left} and the approximate solutions of (14)

are close. As expected, outside the bandgap the absolute value of the transmission is equal to 1. In addition, both Fig. 7 (b) and (c) highlight the amount of approximation of Φ_{left} for a range of perturbation $3 \cdot 10^{-4} < \epsilon < 8 \cdot 10^{-4}$.

For the case of a damped chain, we apply a Rayleigh damping model with modal damping ratios $\zeta_1 = 17\%$ and $\zeta_2 = 3.8\%$, leading to the viscous damping parameters $c = 907.2$ N·s/m and $c_R = 7.4304 \cdot 10^3$ N·s/m. To measure the degree of approximation, we derive an approximate expression for the dispersion law of a damped nonlinear chain, employing the same assumptions of [61]:

$$\begin{aligned} m m_R\,\omega^4 + \left[-c_R\,(m+m_R)\,i + 2\,c\,m_R\,\sigma\,i\right]\omega^3 \\ +\left[2\,k\,m_R\,\sigma - 2\,G(\kappa d)\,k_{NL}\,m_R\,U^2 - k_R\,(m+m_R) + 2\,c\,c_R\,\sigma\right]\omega^2 \\ +\left(2\,i\,G(\kappa d)\,c_R\,k_{NL}\,U^2 - 2\,c\,k_R\,\sigma\,i - 2\,c_R\,k\,\sigma\,i\right)\omega \\ -2\,k_R\left(k\,\sigma - G(\kappa d)\,U^2\,k_{NL}\right) = 0, \end{aligned} \tag{15}$$

where $\sigma = \cos(\kappa d) - 1$. The relevant results are shown in Fig. 8 for U = 15 mm.

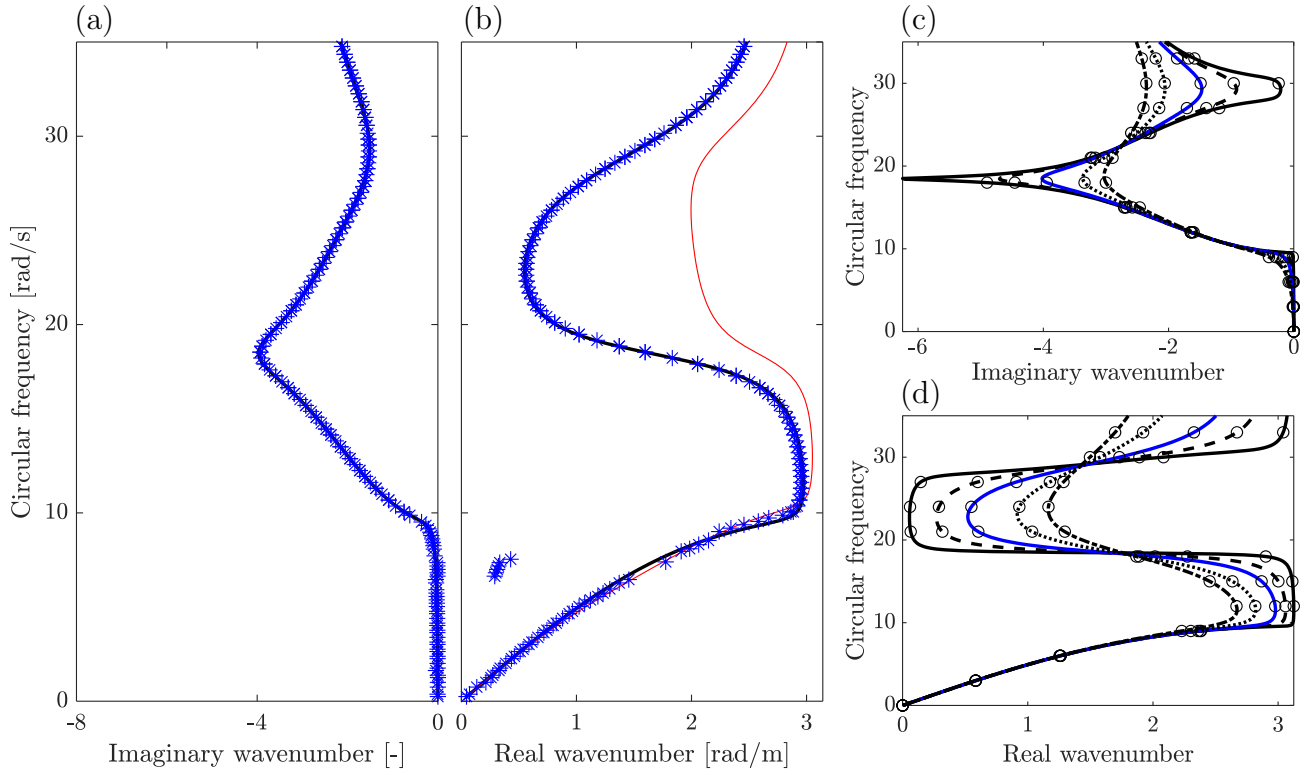

Figure 8: Damped periodic system identification: (a) imaginary components κ_i and (b) real components κ_r of the wavenumbers. The numerical results are compared to the analytical solution provided by (15). The black and red curves define the linear and *nonlinear dispersion curve* from Eq. (15), respectively, while the blue markers represent the ID solutions. Identification of: (c) imaginary wavenumbers and (d) real wavenumbers for a weakly nonlinear case with U = 5 mm and varying values of damping factor D. In particular, the blue curve represents $D = 1$, the solid black curve $D = 0.1$, the dashed black curve $D = 0.5$, the tightly-dashed black curve $D = 2$, and the alternately small-big dashed black curve $D = 3$. Finally, the black circles denote the relevant ID solutions.

The two branches of the undamped curve depicted in Fig. 5 (b) here merge into a single curve, Fig. 8 (b), that features the characteristic S-shape of damped resonant metamaterials [31]. This additional branch is characterized by a backward slope determined by a negative group velocity [21]. However, the presence of damping does not impair the identification procedure; Figs. 8 (c) and (d), highlight various curves characterized by a different damping multiplication factor D. The analytical prediction (15) initially agrees with the identified curve in Fig. 8 (b), but loses accuracy when the group velocity becomes negative; in fact, (15) fails at about 10 rad/s, when the wavenumber is complex, i.e., the bandgap of the undamped case.

3.2. Parametric identification based on subspace identification techniques

An extensive body of literature by De Moor and Van Overschee delves into subspace identification (SI) methods. Refer, among others, to their noteworthy articles from the '90s [68, 69, 70]. Clearly, SI methods have been used also for nonlinear SI in structural dynamics [71, 72]; therefore, we propose their application to nonlinear periodic systems. SI methods exploit the QR factorisation and/or the Singular Value Decomposition by means of oblique projections of the row space of matrices. The unknowns of the method are both the model order and the state-space matrices of a discrete time model in state-space, with s measurements, as follows:

$$\begin{cases} \boldsymbol{x}_{k+1} = \mathbf{A}\boldsymbol{x}_k + \mathbf{B}\boldsymbol{v}_k + \boldsymbol{w}_k, \\ \boldsymbol{y}_k = \mathbf{C}\boldsymbol{x}_k + \mathbf{D}\boldsymbol{v}_k + \boldsymbol{z}_k, \end{cases} \tag{16}$$

where, $\boldsymbol{x} \epsilon \mathrm{R}^n$, $\boldsymbol{y} \epsilon \mathrm{R}^l$ and $\boldsymbol{v} \epsilon \mathrm{R}^m$ are the state-space vector, the output vector and the input vector, respectively; $\boldsymbol{w}$ and $\boldsymbol{z}$ are the process and measurement vectors; $\mathbf{A} \epsilon \mathrm{R}^{nxn}$ and $\mathbf{B} \epsilon \mathrm{R}^{nxm}$ are the system and the input matrices; $\mathbf{C} \epsilon \mathrm{R}^{lxn}$ and $\mathbf{D} \epsilon \mathrm{R}^{lxm}$ are the output and the direct feedthrough matrix. The characters n, l and m symbolize the order of the system, the number of outputs and the number of inputs, respectively. The input and output data are collected in block Hankel matrices. To identify the unknown state-space matrices, we implemented the so-called "subid" algorithm developed by Van Overschee and De Moor [68, 69, 70]. Once the state-space matrices $\mathbf{A}, \mathbf{B}, \mathbf{C}$ and $\mathbf{D}$ have been identified, we need to transform the system from discrete to continuous. In this respect, we adopted the zero-order hold time conversion method, which assumes that the control inputs are piecewise constant over the sampling period. The corresponding time-invariant

continuous system is described by the following state-space model:

$$\begin{cases} \dot{\boldsymbol{x}} = \mathbf{A}_c\, \boldsymbol{x} + \mathbf{B}_c\, \boldsymbol{v}, \\ \boldsymbol{y} = \mathbf{C}\, \boldsymbol{x} + \mathbf{D}\, \boldsymbol{v}. \end{cases} \tag{17}$$

Once the state-space matrices $\mathbf{A}_c, \mathbf{B}_c, \mathbf{C}$ and $\mathbf{D}$ are found, the so-called "extended" transfer function $\mathbf{H}_E(\omega)$ of the nonlinear system can be defined as:

$$\mathbf{Y}(\omega) = \mathbf{H}_E(\omega)\, \mathbf{V}(\omega) = \Big[\mathbf{D} + \mathbf{C}(i\omega\mathbf{I} - \mathbf{A}_c)^{-1}\, \mathbf{B}_c\Big]\mathbf{V}(\omega), \tag{18}$$

where $\mathbf{Y}(\omega)$ and $\mathbf{V}(\omega)$ are the Fourier transforms of the output and the input, respectively. According to Marchesiello and Gandino [72], we can derive the unknown mechanical parameters, i.e., the linear stiffness k and the nonlinear k_{NL}, as follows. The system of EoM of a nonlinear system with h degrees of freedom reads:

$$\mathbf{M}\ddot{\boldsymbol{u}}(t) + \mathbf{C}\dot{\boldsymbol{u}}(t) + \mathbf{K}\boldsymbol{u}(t) + \sum_{j=1}^{p} \mu_j \boldsymbol{L}_{nj} g_j(t) = \boldsymbol{f}(t), \tag{19}$$

where $\mathbf{M}, \mathbf{C}$ and $\mathbf{K}$ are the mass, damping and linear stiffness matrices, respectively; $\boldsymbol{u}(t)$ is the absolute displacement vector and $\boldsymbol{f}(t)$ the linear force vector. The nonlinear term is expressed as the sum of p components, each of them depending on the scalar nonlinear function g_j and on the scalar nonlinear parameter μ_j through the vector $\boldsymbol{L}_{nj}$; it is composed by only $1, 0$ or -1, depending on the location of the nonlinear element. The function g_j defines the class of nonlinearity. As we deal with a cubic restoring force, see Eq. (7), we can move the nonlinear term to the right-hand side, and consider the nonlinear force as an internal feedback force. The system parameters k and k_{NL} to be identified are contained in the invariant matrix $\mathbf{H}_E(\omega)$, as shown by (18). As a result, one can derive the parameters k and k_{NL} from the estimated transfer function [71], as follows:

$$\mathbf{H}_E(\omega) = \Big[\mathbf{H} \quad \mathbf{H}\,\mu_1 \boldsymbol{L}_{n1} \quad \ldots \quad \mathbf{H}\,\mu_p \boldsymbol{L}_{np}\Big], \tag{20}$$

where $\mathbf{H}$ is the linear transfer function. For zero frequency, the estimated $\mathbf{H}_E$ finally becomes:

$$\mathbf{H}_E(\omega = 0) = \Big[\mathbf{K}^{-1} \quad \mathbf{K}^{-1}\,\mu_1 \boldsymbol{L}_{n1} \quad \ldots \quad \mathbf{K}^{-1}\,\mu_p \boldsymbol{L}_{np}\Big]. \tag{21}$$

3.2.1. *Application with a white noise input*

Herein, we present the application of the SI method applied to the RS depicted in Fig. 3 when the input is a white noise (WN). The boundary conditions are applied to the left- and right-side of the RS in the form of a zero-mean Gaussian random input whose root mean squares are $U_{left} = 80\,mm$ and $U_{right} = 40\,mm$, respectively, as depicted in Fig. 9.

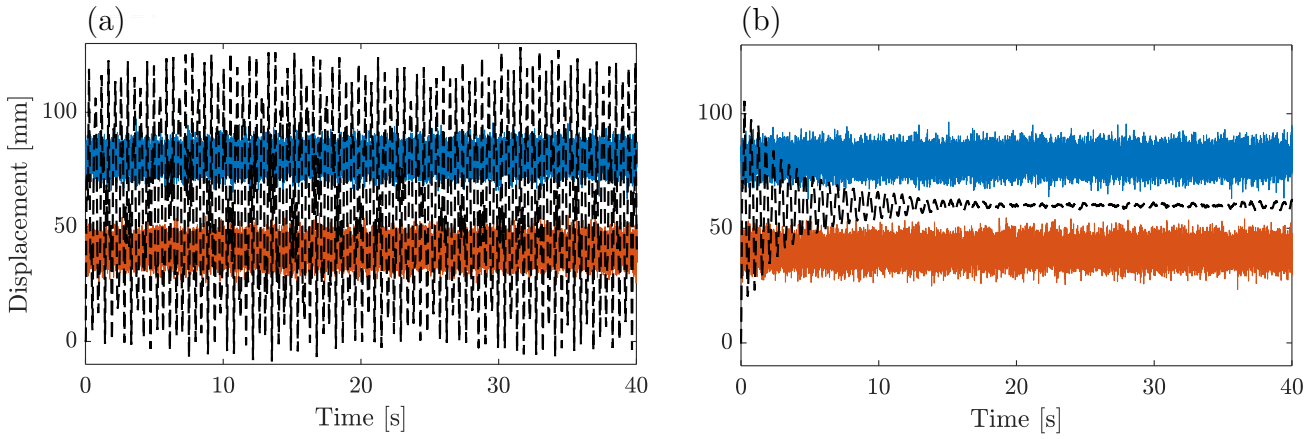

Figure 9: Gaussian white noise (WN) displacements applied to the boundaries of the RS and relevant output: (a) undamped case and (b) damped case. The blue signal defines the WN applied to the left boundary, while the orange signal represents the WN on the right boundary. The black signal corresponds to the output.

Fig. 9 (a) depicts input and output of the undamped case, while Fig. 9 (b) refers to the damped case. For clarity, the output response of the resonator is omitted from display, despite being included in the output vector and, consequently, in the Hankel matrix. Similarly, the input and output velocities, which are also encompassed within the Hankel matrix, are not shown for the sake of brevity. To assess measurement noise effects, we introduced varying levels of WN into the output. In Fig. 10, one simulation illustrates good agreement between the identified system's output and the original.

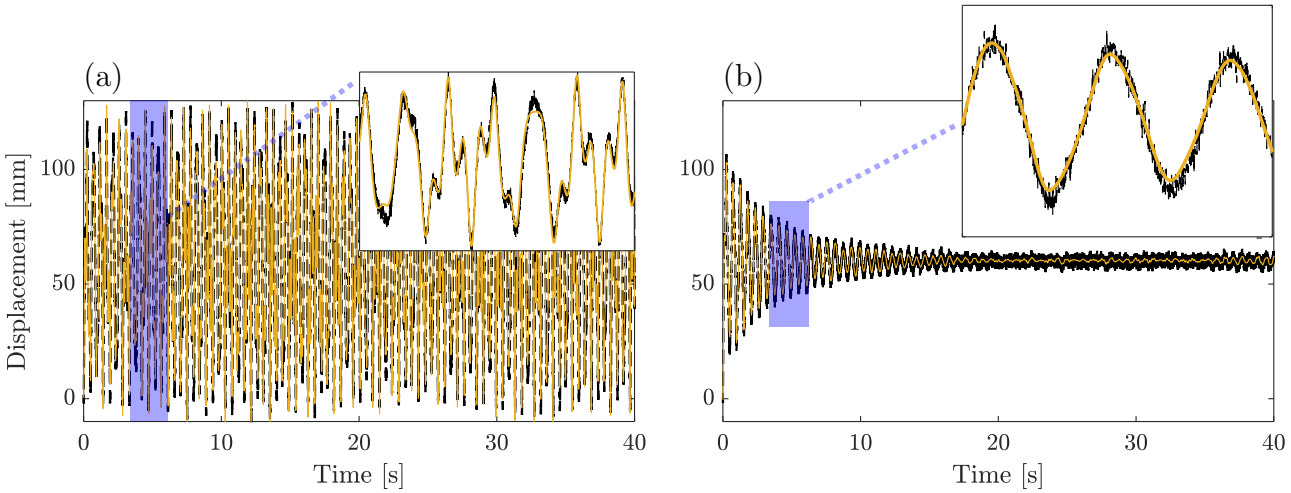

Figure 10: Comparison between outputs of the identified model and of the original output: (a) undamped case, (b) damped case. The black signal corresponds to the original output with 1% of WN, while the yellow signal defines the simulated (identified) output.

The added noise amounts to a certain percentage of the root mean square of the entire output. The errors associated to the identified parameters k and k_{NL} of the undamped RS after 200 simulations for each output noise level are collected in Tab. 1. One may conclude that the involved errors are small w.r.t. noise.

Noise level [%]	**Mean (Err k) [%]**	**Std (Err k) [%]**	**Mean (Err $\mathbf{k_{NL}}$) [%]**	**Std (Err $\mathbf{k_{NL}}$) [%]**
0.1	0.0893	0.0045	0.2491	0.0570
0.3	0.0878	0.0146	0.2237	0.1533
0.5	0.0914	0.0246	0.2749	0.1999
1	0.0888	0.0410	0.6224	0.4393
2	0.1002	0.0716	2.8645	1.2136
3	0.1238	0.0968	6.2799	1.7438

Table 1: Error values w.r.t. the parameters k and k_{NL} after 200 simulations for each noise level, undamped case.

Similarly, mean and standard deviation of errors for the identification of the damped RS are listed in Tab. 2 for the damped case. One may argue that also in this case the involved errors are small.

Noise level [%]	**Mean (Err k) [%]**	**Std (Err k) [%]**	**Mean (Err $\mathbf{k_{NL}}$) [%]**	**Std (Err $\mathbf{k_{NL}}$) [%]**
0.1	0.0039	0.0015	1.2105	0.1623
0.3	0.0045	0.0035	1.9626	0.5771
0.5	0.0066	0.0049	1.6027	0.8415
1	0.0108	0.0086	1.4348	1.0306
2	0.0224	0.0167	8.0911	3.1529

Table 2: Error values w.r.t. the parameters k and k_{NL} after 200 simulations for each noise level, damped case.

3.2.2. Application with Floquet-Bloch conditions

The identification of periodic nonlinear systems by means of the SI ideally requires both a rich frequency content of the input and of the amplitude [73]. To meet these requirements while keeping a harmonic excitation to guarantee the application of F-B boundary conditions, we considered a harmonic input corrupted with a Gaussian WN and shifted to a non zero mean value U_{left}, i.e.,

$$\begin{aligned} u_{left} &= U_{left} + U_{left} \exp(i\omega t), \\ u_{right} &= U_{left} + (u_{left} - U_{left}) \exp(2i\kappa d). \end{aligned} \tag{22}$$

An example is shown in Fig. 11, for $U_{left} = 5$ mm and $\omega = 10$ rad/s.

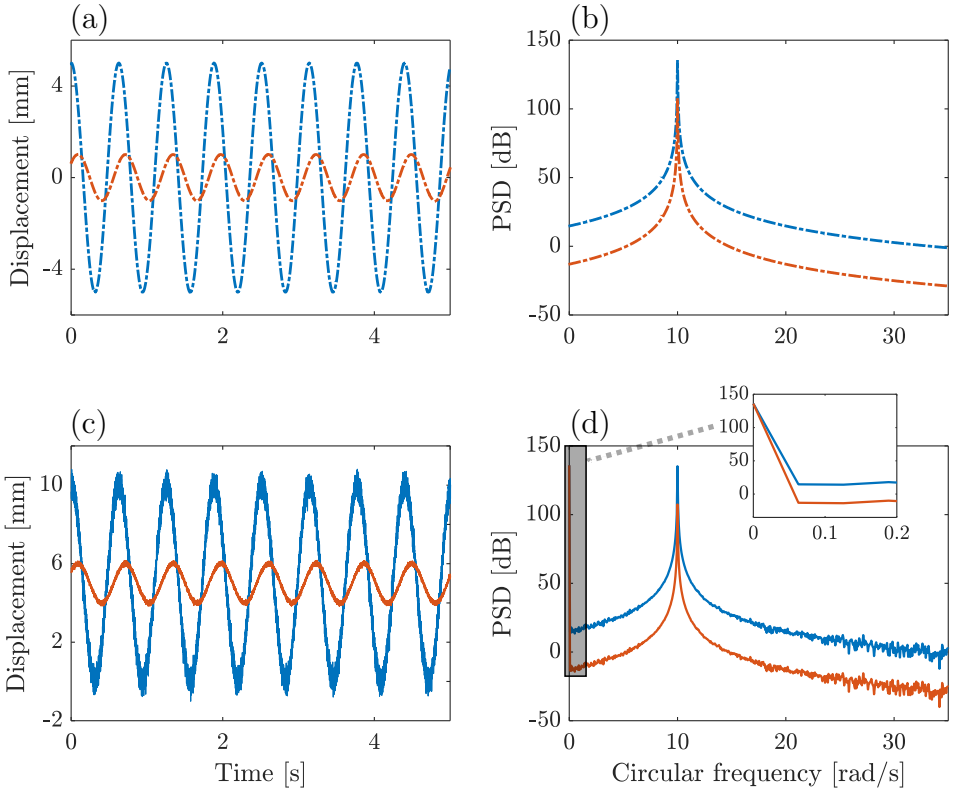

Figure 11: Original F–B input signals and modified F–B signals to left and right boundaries of the RS, and relevant power spectral densities (PSDs). (a) Original inputs; (b) PSDs of the original inputs; (c) Modified (shifted) inputs with WN; (d) PSDs of the modified inputs. The blue signals correspond to the input at the left boundary, while the orange signal represents the input on the right boundary.

A careful reader can notice that the power spectral densities (PSDs) of both the original and modified signals remain essentially unchanged with a favourable frequency enrichment. Furthermore, the close-up box shows that the addiction of the value U_{left} to the original excitation causes the PSD to increase at zero frequency due to the δ Dirac function.

Both results and relevant errors associated with the application of the SI method are reported in Tab. 3 and Tab. 4 for the undamped and damped case, respectively. For these cases, we selected an amplitude $U_{left} = 10\,mm$ and three circular frequencies of the identified dispersion curves depicted in Fig. 4 and Fig. 8. The complex wavenumbers were also taken from the identified dispersion curves.

Circ. frequency [rad/s]	**Wavenumber [rad/m]**	**Err k [%]**	**Err $\mathbf{k_{NL}}$ [%]**
3	1.3+0.005i	1.233	3.490
16	1.4+3.217i	0.992	2.357
30	2.2+0.225i	1.814	4.004

Table 3: Error values w.r.t. the parameters k and k_{NL} for amplitudes $U_{left} = 5\,mm$ and $SNR = 20\,dB$, in the undamped case.

Circ. frequency [rad/s]	**Wavenumber [rad/m]**	**Err k [%]**	**Err k_{NL} [%]**
6	1.3+0.037i	1.151	3.040
16	1.9+3.111i	0.855	1.961
30	1.9+1.546i	0.670	2.005

Table 4: Error values w.r.t. the parameters k and k_{NL} for amplitudes $U_{left} = 5\,mm$ and $SNR = 20\,dB$, in the damped case.

We can argue that even in such instances identification errors are still limited. Clearly, the amount of errors can be further limited by a careful reduction of the SNR that characterizes the harmonic input and the added WN.

3.3. Identification of dispersion curves for a mass-in-mass system with nonlinear resonators

To further demonstrate the generality of the proposed method, we briefly report on the identification of a periodic mass-in-mass system with nonlinear springs connecting the resonators to the main masses. The relevant RS of such a system is depicted in Fig. 12.

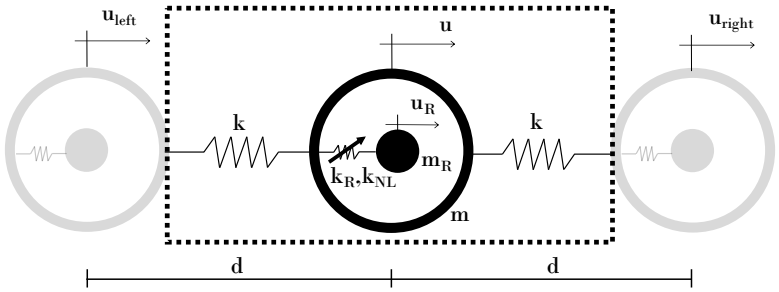

Figure 12: Reference subsystem (RS) for the 1D mass-in-mass metamaterial with embedded nonlinear resonators.

The relevant system of EoMs reads:

$$\begin{cases} m\ddot{u} + k\big(2u - u_{left} - u_{right}\big) + k_R\big(u - u_R\big) + k_{NL}\big(u - u_R\big)^3 = 0, \\ m_R\ddot{u}_R + k_R\big(u_R - u\big) + k_{NL}\big(u_R - u\big)^3 = 0, \end{cases} \tag{23}$$

where k_{NL} denotes the nonlinear spring constant. while all the parameters are equal to the system investigated in Subsection 3.1, the nonlinear spring is 1393.2 MN/m^3, such that $\frac{k_{NL}U^3}{k_R U}$ is equal to 13% for U = 10 mm, similarly to the case of Fig. 6 (a). The F–B boundary conditions are imposed according to (8) and (9), and the free wave identification procedure is carried out following Fig. (2).

We can find a reference solution by applying a perturbation approach similar to the one detailed in Appendix A. First, we consider a Fourier series for both u and u_R. Then, after development

and separation of the equations in the ϵ^0 and ϵ^1 orders, we assume a harmonic regime for u and u_R and determine the correction term, $\bar{\omega}_1$, which is added to the linear frequency, $\bar{\omega}_0$. The resulting nonlinear dispersion curve reads:

$$\bar{\omega} = \bar{\omega}_0 + \epsilon\,\bar{\omega}_1, \tag{24}$$

$$(\bar{\omega}_0)^2 = \frac{1 + \frac{m_R}{m} + 4\,\frac{m_R\,k}{k_R\,m}\sin^2(\frac{\mu}{2}) - \sqrt{\left(1 + \frac{m_R}{m} + 4\,\frac{m_R\,k}{k_R\,m}\sin^2(\frac{\mu}{2})\right)^2 \pm 16\frac{m_R\,k}{k_R\,m}\sin^2(\frac{\mu}{2})}}{2\frac{m_R\,k}{k_R\,m}}, \tag{25}$$

$$\bar{\omega}_1 = \frac{3\frac{k_{NL}}{k}|U|^2}{8}\,\frac{\left(\frac{m_R\,k}{k_R\,m}\right)^4\bar{\omega}_0^7}{\left(1 - \frac{m_R\,k}{k_R\,m}\bar{\omega}_0^2\right)^2\left(\frac{m_R}{m} + (1 - \frac{m_R\,k}{k_R\,m}\bar{\omega}_0^2)^2\right)}, \tag{26}$$

where $\bar{\omega}$ represents the nondimensionalized nonlinear dispersion curve over $\sqrt{k/m}$, $\mu = \kappa d$ is the propagation constant, and ϵ is the perturbation parameter. The current approach shares similarities with the works by Lazarov et al. [31] and by Campana et al. [41], where ϵ does not assume a physical meaning. As depicted in Fig. 13, the identified solutions reside in a range of values of ϵ.

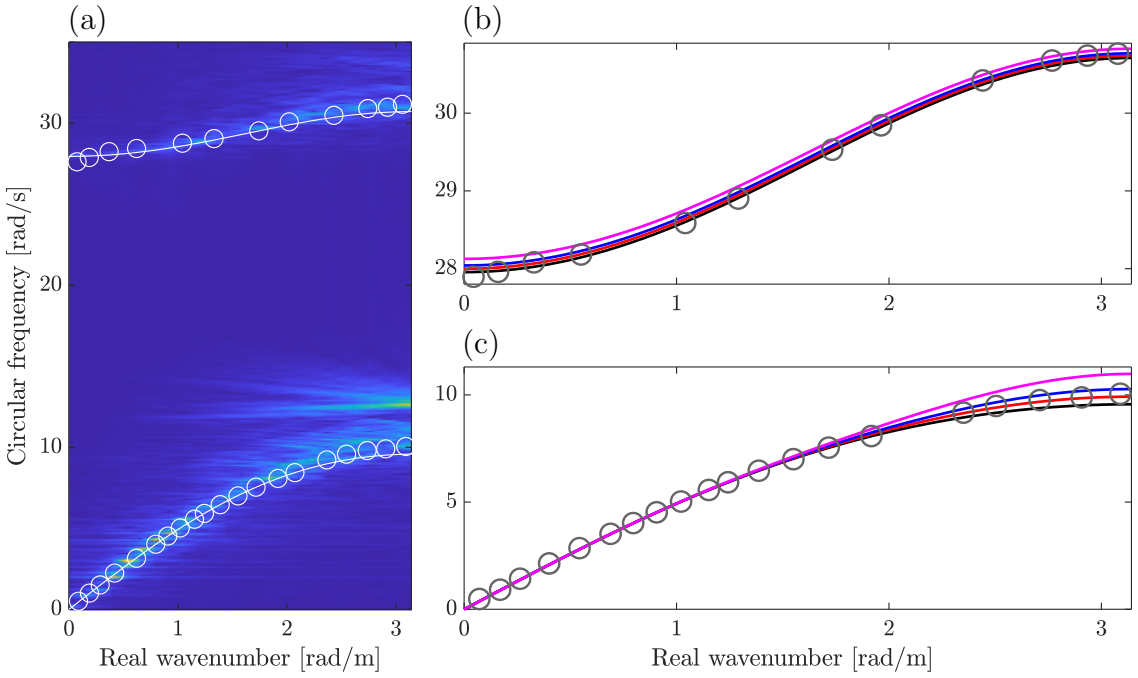

Figure 13: Mass-in-mass system with nonlinear resonators: (a) finite lattice dispersion curves from the 2D-FFT for U = 10 mm, (b) close-up on the optical branch of the dispersion curves from Eq. (24), and (c) close-up of the acoustic branch. (b) The black curve defines the linear dispersion curve ($\epsilon = 0$), while the red, blue, and magenta curves correspond to $\epsilon = 1 \cdot 10^{-3}$, $\epsilon = 2 \cdot 10^{-3}$, and $\epsilon = 4 \cdot 10^{-3}$, respectively. (c) The red, blue, and magenta curves correspond to $\epsilon = 0.1$, $\epsilon = 0.2$, and $\epsilon = 0.4$, respectively. The circles represent the ID solutions.

For an amplitude U = 10 mm, the approximation in the optical branch is found in a range of perturbation $1 \cdot 10^{-3} < \epsilon < 4 \cdot 10^{-3}$; whereas for the acoustic branch the range is $1 \cdot 10^{-1} < \epsilon < 2 \cdot 10^{-1}$. For brevity, the plot for U = 15 mm is not reported, but the range of perturbation reads $8 \cdot 10^{-4} < \epsilon < 2 \cdot 10^{-3}$ for the optical branch, and $6 \cdot 10^{-2} < \epsilon < 1 \cdot 10^{-1}$ for the acoustic branch.

4. Linear mass-in-mass system: a simple version of the identification procedure

The identification strategy outlined in Section 2 and applied in Section 3 is easily applicable to linear systems. This section reports on its application to a linear undamped mass-in-mass system and represents a simplified application. The true advantage of the proposed simple procedure lies in its suitability for the initial stages of experimental processes, where the immediate identification of the imaginary wavenumber is not a primary concern. The simple procedure ensures a rapid implementation without requiring extensive computations to support the experiment. The dispersion curves are identified in Section 4.1, while the relevant mechanical characteristics are identified in Section 4.2.

4.1. Dispersion curves identification

The linear resonant undamped RS of interest is shown in Fig. 14.

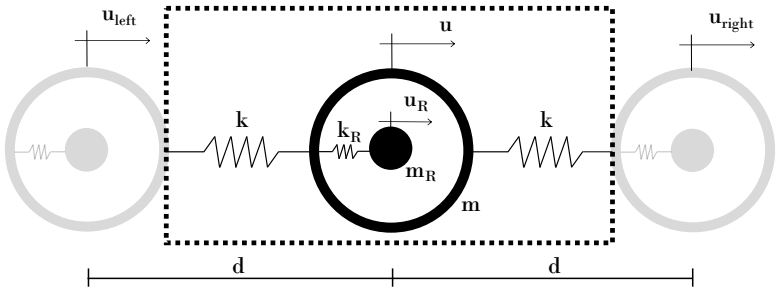

Figure 14: Reference subsystem (RS) for a linear resonant undamped 1D chain.

The system of equations of motion (EoM) for the external mass and the resonator are as follows:

$$\begin{cases} m\ddot{u} + k\big(2u - u_{left} - u_{right}\big) + k_R\big(u - u_R\big) = 0 \\ m_R\ddot{u}_R + k_R\big(u_R - u\big) = 0 \end{cases} \tag{27}$$

where u and u_R denote the displacements of the external mass m and resonator m_R, respectively; k and k_R are the stiffnesses; and the dot indicates the derivative with respect to time. For an undamped periodic system, the wavenumber is real in the passband, with no amplitude decay, and purely imaginary in the bandgap. Therefore, upon application of the F–B boundary conditions (8) and (9), the identification of the propagating waves requires finding the frequency ω for which the

output satisfies the following equations:

$$\begin{cases} |FRF| = \left|\frac{U}{U_{left}}\right| = |\exp(i\kappa d)| = 1 \\ \\ \Delta\phi = \tan^{-1}\frac{\Im(U/U_{left})}{\Re(U/U_{left})} = \kappa d \end{cases} \tag{28}$$

where U defines the amplitude of the output and $\Delta\phi$ the relative phase between the left input displacement and the output. It is important to emphasize that the system (28) is analogous to (4) for an undamped structure, the wavenumber being either real or imaginary. Consequently, while the use of the procedure illustrated in Fig. 2 remains viable, it becomes possible to conceive a simple dispersion curve identification procedure, encompassing the subsequent steps:

- Step I: the RS is excited in displacement control with (8) and (9) for a fixed amplitude U_{left}, a given κ and a first trial frequency ω, selected to be close to zero;
- Step II: the output amplitude U is evaluated in the steady state regime, and the ratio $|\frac{U}{U_{left}}|$ is then computed;
- Step III: Steps I and II are repeated for increasing values of ω until the first solution to (28) is found. This solution (κ, ω) lies on the acoustic branch;
- Step IV: the input frequency ω is further increased, and Step III is repeated until a second solution that satisfies (28) is found. The second solution (κ, ω) lies on the optical branch;
- Step V: Steps I–IV are repeated for the desired $\bar{\kappa}$ in the range $0, \pi/d$.

A short sampling value of ω is recommended to avoid the accidental missing of the acoustic or optical branch. Note that the two branches can be discriminated by considering the relative phase between the external mass and resonator; the two masses vibrate in-phase along the acoustic branch and in phase opposition along the optical branch.

The mechanical properties of the RS are the same as the nonlinear discrete structure investigated in Section 3, with $k_{NL} = 0$. To compare the numerical results with a reference solution, the FRF of the system of interest was obtained in closed form by combining Eqs. (8) and (9) with the linear system of EoMs (27), i.e.,

$$FRF = \frac{k\,(1 + e^{2i\kappa d})}{-m\omega^2 + 2k - \frac{k_R^2}{k_R - m_R\omega^2} + k_R}. \tag{29}$$

Likewise, the application of the F–B theorem to the system of EoMs (27) and a few manipulations leads to the well-known analytical dispersion relation of a locally resonant periodic lattice [21].

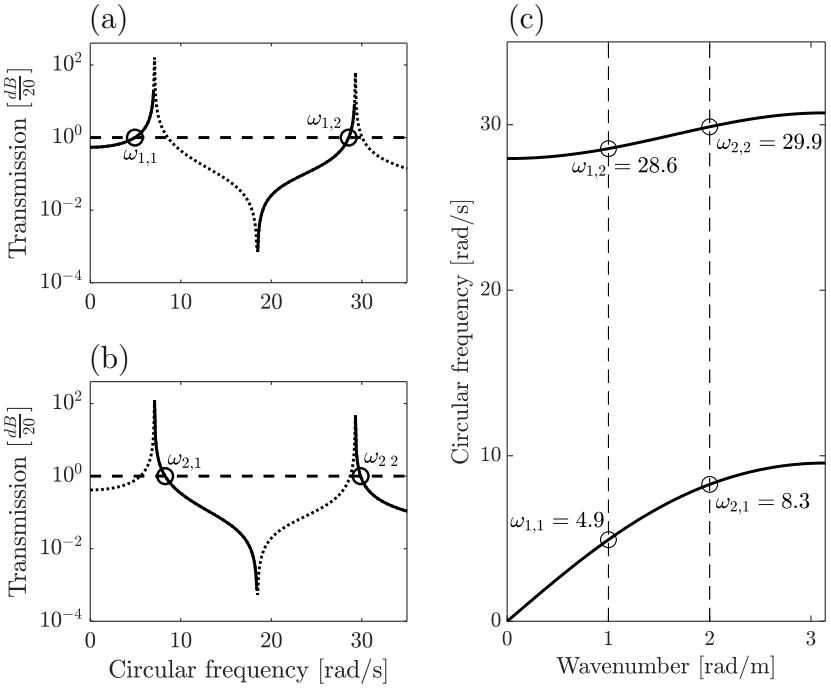

Figure 15: Analytical $|FRF|$ (29) for (a) a wavenumber $\kappa = 1\,\text{rad/m}$ and (b) a wavenumber $\kappa = 2\,\text{rad/m}$; (c) analytical dispersion curves of the linear periodic undamped chain. The dotted curves in (a) and (b) indicate the range where $\Im(U) < 0$, whereas the solid lines are for $\Im(U) > 0$. The black circles represent the identified numerical solutions.

The FRF values computed using (29) for $\kappa = 1$ and $\kappa = 2$ rad/m are shown in Figs. 15 (a) and (b), respectively. In the same plot, the frequency values ω satisfying (28) are marked with circles. As expected, the transmissions shown in Figs. 15 (a) and (b) decrease after each resonance, with $FRF \to 0$ for $lim\ \omega \to \infty$. This may be considered a warning when the optical branch is accidentally passed during the identification process. Note also that the wavenumber is non-zero; therefore, the transmission does not equal 1 for a zero frequency. On the other hand, Eq. (29) confirms that $\frac{U}{U_{left}} = 1$ for $\omega = 0$ and $\kappa = 0$. The amplitudes of the transmissions $|\frac{U}{U_{left}}|$ for those solutions that satisfy (28) are compared with the analytical $|FRF|$ of (29) in Fig. 16 (a); the same set of solutions is plotted in Fig. 16 (b) in terms of relative phase.

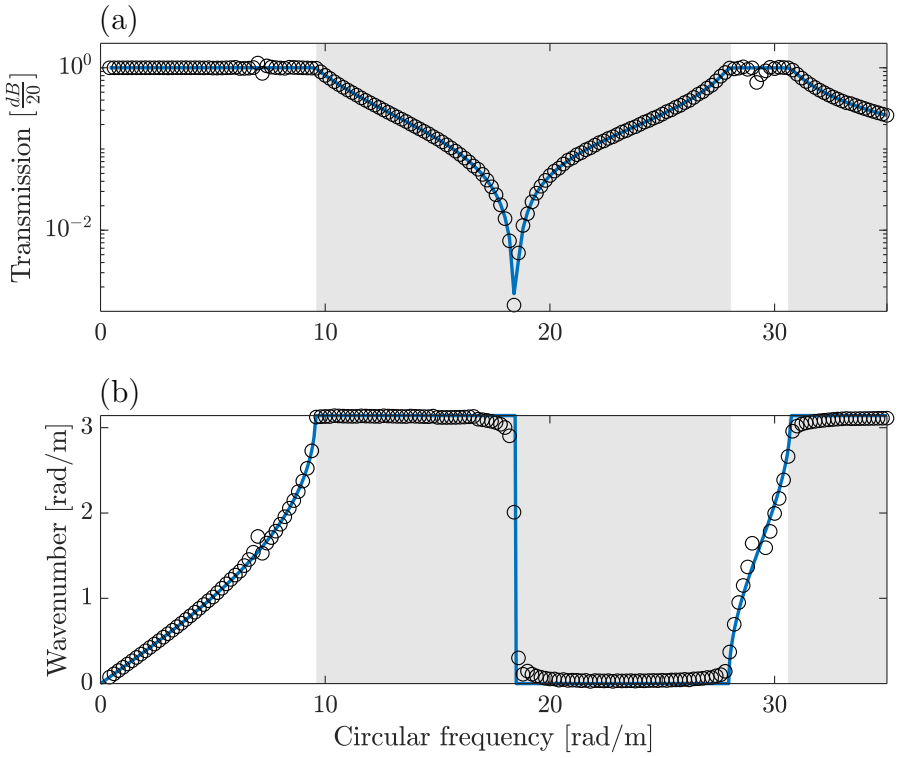

Figure 16: Comparison between the analytical and numerical solutions: (a) absolute value of the transmissions, and (b) the relative phases $\Delta\phi$ between the output and the input. (a) The blue curve defines the analytical solution $|FRF|$ from Eq. (29), while the circles correspond to the numerical values $|\frac{U}{U_{left}}|$. (b) The blue curve represents the analytical solution $tan^{-1}\frac{\Im(FRF)}{\Re(FRF)}$, while the circles correspond to the numerical values $tan^{-1}\frac{\Im(U/U_{left})}{\Re(U/U_{left})}$. The gray areas highlight the bandgaps.

As predicted by (28), the transmission is equal to 10^0 outside the bandgaps where purely propagative waves exist.

4.2. Parametric identification

Once the dispersion curves are obtained, the mechanical parameters identification of the linear structure is straightforward. In particular, each point of the dispersion curve $\kappa - \omega$ satisfies the following eigenproblem:

$$det(\mathbf{K}(\kappa) - \omega^2\mathbf{M}) = 0, \tag{30}$$

where $\mathbf{K}(\kappa)$ is the wavenumber-dependent stiffness matrix of the linear infinite lattice and $\mathbf{M}$ is the mass matrix [21]. Therefore, it is possible to identify the four unknown mechanical parameters of the system, namely, m, m_R, k, and k_R, by solving a system of four equations (30):

$$det\left(\begin{bmatrix} 2k^{ID}\big(1-\cos(\kappa d)\big)+k_R^{ID} & -k_R^{ID} \\ -k_R^{ID} & k_R^{ID} \end{bmatrix} - \omega^2 \begin{bmatrix} m^{ID} & 0 \\ 0 & m_R^{ID} \end{bmatrix}\right) = 0, \tag{31}$$

where the superscript, *ID*, denotes the parameters to be identified. Consequently, we retrieved a system of four equations for the four unknowns m^{ID}, m_R^{ID}, k^{ID} and k_R^{ID}. We arbitrarily selected two

wavenumbers and the corresponding two pairs of frequencies from the identified dispersion curve; see, for example, the circles in Fig. 15 (c). Thus, the inverse eigenproblem of Eq. (31) leads us to the identification of four unknowns.

5. Linear continuous bi-material beam: identification of dispersion curves for axial and flexural vibrations

The proposed identification procedure is adaptable to one-dimensional waveguides. In this section, we utilize a bi-material beam as a reference [48]. The beam operates within a frequency range higher than those relevant to the discrete cases investigated thus far. This validates the effectiveness of the proposed identification procedure across various frequency ranges.

The waveguide is made by repetitions of steel and lead parts and is analytically modeled with the Euler–Bernoulli beam theory. More specifically, for a straight axis beam x, the axial vibrations entail:

$$q(x,t) = Q\exp(i\kappa_q x + i\omega t), \tag{32}$$

$$F_q(x,t) = EA\frac{\partial q}{\partial x}, \tag{33}$$

where q is the axial displacement, Q the amplitude and F_q the axial force. The relevant wavenumber in (32) is $\kappa_q = \sqrt{(\rho\omega^2)/E}$, where E is the Young modulus and ρ is the density. Instead, flexural vibrations entail:

$$w(x,t) = W\exp(i\kappa_w x + i\omega t), \tag{34}$$

$$\theta(x,t) = \frac{\partial w}{\partial x}, \tag{35}$$

$$M(x,t) = EJ\frac{\partial^2 w}{\partial x^2}, \tag{36}$$

$$V(x,t) = -\frac{\partial M}{\partial x}, \tag{37}$$

where w is the transversal displacement, U the amplitude, θ the rotation, M the bending moment and V the shear force. The wavenumber in (34) is $\kappa_w = (\rho A\omega^2)/EJ$, where J and A are the moment of inertia and the area of the cross-section, respectively. The RS of the one-dimensional waveguide is constructed upon the n^{th} unit cell and is depicted in Fig. 17.

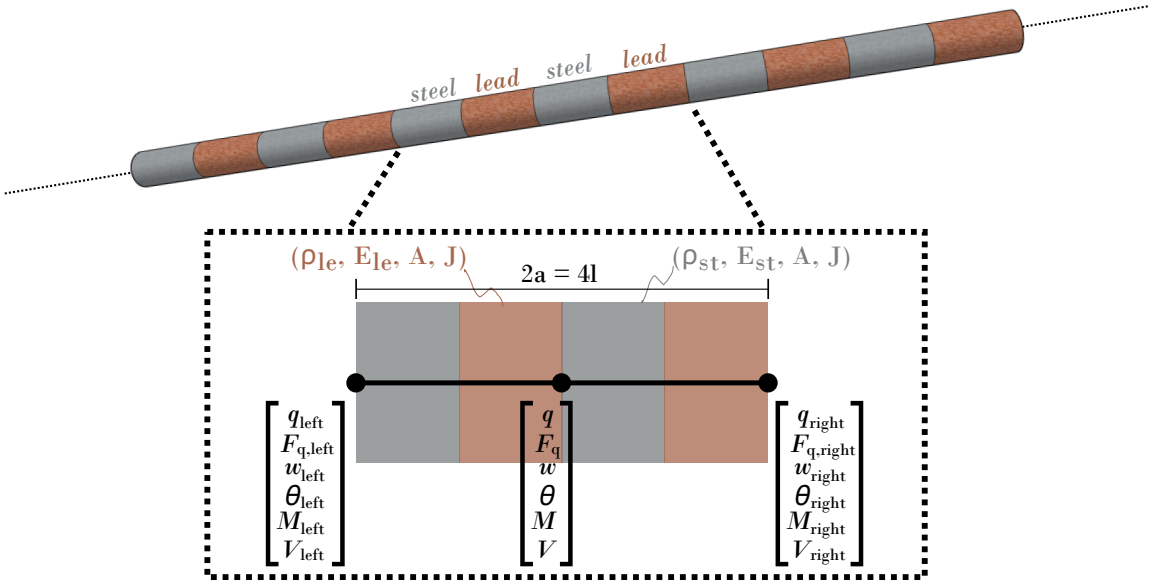

Figure 17: Reference subsystem (RS) for the continuous beam constituted by periodic parts of steel and lead.

To carry out the dispersion curve identification procedure, we use the same approach as in Section 2, but we treat the axial and flexural as separate problems, because the relevant equations of motion (32)-(37) are decoupled. As in the discrete case, only one wavenumber is needed to characterize the dispersion curve of an Euler–Bernoulli beam. Nonetheless, differently from the spring-mass chains investigated in the previous sections, the analysis of a continuous beam requires the incorporation of rotations and boundary forces, including axial forces, shear forces, and bending moments, in addition to displacements.

More specifically, for axial vibrations, the F–B boundary conditions are imposed on the RS as follows:

$$q_{left} = Q_{left} \exp(i\omega t), \tag{38}$$

$$F_{q,left} = EA\, i\kappa_q Q \exp(i\omega t), \tag{39}$$

$$q_{right} = q_{left} \exp(2i\kappa_q a), \tag{40}$$

$$F_{q,right} = F_{q,left} \exp(2i\kappa_q a), \tag{41}$$

where Q_{left} is the amplitude of the imposed displacement. For a given frequency ω, the amplitude

of the output displacement Q must fulfill the following conditions:

$$\begin{cases} FRF_{q,left} = \dfrac{Q}{Q_{left}} = \exp(i\kappa_{q,r}d)\exp(-\kappa_{q,i}d), \\ \\ FRF_{q,right} = \dfrac{Q}{Q_{right}} = \exp(-i\kappa_{q,r}d)\exp(\kappa_{q,i}d). \end{cases} \tag{42}$$

Similarly, for the flexural vibrations, the F–B boundary conditions are imposed to the RS as follows:

$$w_{left} = W_{left}\exp(i\omega t), \tag{43}$$

$$\theta_{left} = i\kappa_w w_{left}, \tag{44}$$

$$V_{left} = EJ\, i\kappa_w^3 w_{left}, \tag{45}$$

$$M_{left} = -EJ\,\kappa_w^2 w_{left}, \tag{46}$$

$$w_{right} = w_{left}\exp(2i\kappa_w a), \tag{47}$$

$$\theta_{right} = \theta_{left}\exp(2i\kappa_w a), \tag{48}$$

$$V_{right} = V_{left}\exp(2i\kappa_w a), \tag{49}$$

$$M_{right} = M_{left}\exp(2i\kappa_w a), \tag{50}$$

where W_{left} is the amplitude of the imposed transversal displacement. To identify the unknown wavenumber for a given input frequency ω, we solve the following system of equations:

$$\begin{cases} FRF_{w,left} = \dfrac{W}{W_{left}} = \exp(i\kappa_{w,r}d)\exp(-\kappa_{w,i}d), \\ \\ FRF_{w,right} = \dfrac{W}{W_{right}} = \exp(-i\kappa_{w,r}d)\exp(\kappa_{w,i}d). \end{cases} \tag{51}$$

To validate the dispersion curve identification procedure, in accordance with [48], material densities of steel and lead, respectively, read $\rho_{st} = 7800\ \mathrm{kg\,m^{-3}}$ and $\rho_{le} = 11300\ \mathrm{kg\,m^{-3}}$, where the subscript st is for steel and le is for lead; Young's moduli are $E_{st} = 200$ GPa and $E_{le} = 13$ GPa. The cross-section is the same for both materials, thus $A = 0.7854\ \mathrm{m^2}$ is the cross-sectional area, $J = 0.0491\ \mathrm{m^4}$ is the moment of inertia, and $l = 1$ m is the length of the single material beam part. The continuous RS is discretized with 15 nodes in agreement with the Euler–Bernoulli theory and by means of a consistent mass matrix.

The reference solution is obtained through the well-established transfer matrix method, widely used for calculating the band structure of 1D periodic structures [48, 74, 75]. Details of the implementation of the transfer matrix method using the beam theory equations Eqs.(32)-(37) are provided in Appendix B. Fig. 18 reports the results of the identification approach and the band structures obtained with the transfer matrix method.

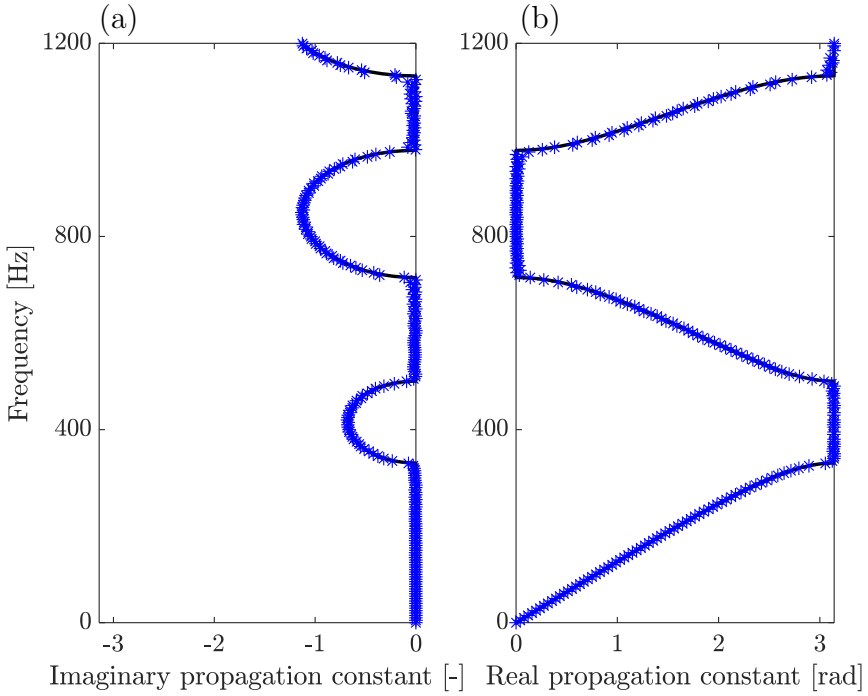

Figure 18: Identification of the continuous bi-material beam in longitudinal vibrations: (a) plot of the imaginary components of the propagation constant and (b) real components of the propagation constant ($\mu_{q,r} = \kappa_{q,r} \cdot a$). The blue markers correspond to the identified solutions and are compared to the black solid dispersion curves obtained through the transfer matrix method.

The dispersion curves are calculated as propagation constant ($\mu = \kappa a$) vs. frequency (f). Given a unit cell length $a = 2$ m, one can note that the results in Fig. 18 match with the axial dispersion curves of Junyi et al. [48].

For completeness, we also considered flexural vibrations and identified the relevant dispersion curves that are depicted in Fig. 19.

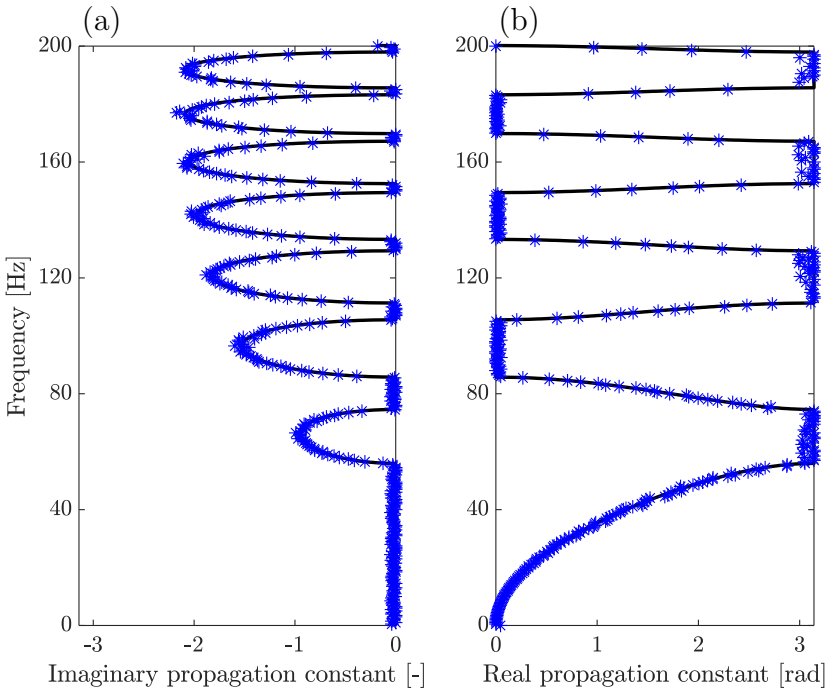

Figure 19: Identification of the continuous bi-material beam in flexural vibrations: (a) plot of the imaginary components of the propagation constant $\mu_{w,i}$ and (b) real components of the propagation constant $\mu_{w,r}$. The blue markers correspond to the identified solutions and are compared to the black solid dispersion curves obtained through the transfer matrix method.

Very small discrepancies between the identified solutions and the transfer matrix solutions are observed in the bandgaps: these errors come from the numerical integration of the EoMs, whereas Junyi et al. [48] employed the analytical solutions of the beam theory to determine the response of the system.

6. Conclusions and future outlook

We have proposed a novel procedure for the identification of linear and nonlinear 1D mechanical metamaterials. We have employed the output of a reference subsystem (RS), comprising the system unit cell and imposing controlled displacements that satisfy the Floquet–Bloch (F–B) periodic conditions. With a few tools, namely the F–B conditions, the frequency response functions (FRFs) of the RS, and the Levenberg–Marquardt algorithm, we have successfully identified the dispersion curves, relevant eigenvalues, and various mechanical parameters for both linear and nonlinear undamped and damped periodic systems. In this respect, a MATLAB routine that implements the identification procedure is available as Supplementary Material.

The main advantages of the proposed identification procedures are: i) they do not operate on finite lattices and, therefore, numerical/experimental issues related to wave reflections, perfectly matched layers, and so on, are avoided; ii) the identification effort is reduced because the procedure

relies on a simple experimentally informed RS; iii) the identification of the dispersion relationship also includes the imaginary part of wavenumbers; iv) the identified wavenumbers of the nonlinear structure depend on the excitation amplitude and, as expected, they are more accurate in the case of weak nonlinearities; this is particularly remarkable in the use of the subspace identification (SI) procedure, where nonlinear stiffness terms have been clearly identified despite the presence of noisy measurements.

The identification procedure has also been implemented for a one-dimensional waveguide, namely a periodic bi-material beam subjected to longitudinal and flexural vibrations. Given the extensive research conducted on these components in recent years [17, 75, 76, 77, 78, 79], the proposed novel identification procedure can easily support their experimental validation.

In sum, we envision the application of this method to the experimental outputs of physical RSs of mechanical metamaterials excited under displacement control. while our method leverages a single displacement measurement of the main mass, future endeavors could explore the benefits of directly measuring the output from nonlinear resonators [80]. Clearly, the physical realization of an RS with the control of parameters that accurately govern nonlinear terms remains challenging and may become critical for experimental systems that need to account for dissipation, higher harmonics, and chaos.

CRediT authorship contribution statement

Fabrizio Aloschi: Conceptualization, Methodology, Software, Validation, Writing. **Oreste Salvatore Bursi**: Conceptualization, Methodology, Resources, Supervision, Review. **Antonio Palermo**: Conceptualization, Methodology, Review. **Alessandro Marzani**: Conceptualization, Methodology, Review.

Declaration of competing interest

The authors declare that they have no known competing financial interests or personal relationships that could have appeared to influence the work reported in this paper.

Acknowledgements

This work received support from the European Union's Horizon 2020 research and innovation program under the Marie Skłodowska-Curie Grant agreement no. INSPIRE - 813424 for all authors.

Furthermore, the second author acknowledges the Italian Ministry of Research in the framework of the project DICAM-EXC (Departments of Excellence 2023-2027, grant L232/2016).

Appendix A. Definition of an FRF for the nonlinear periodic system

To support the developments in Section 3, this subsection provides an analytical expression for the FRF of Eq. (13). To this end, we recall the system of EOMs relevant to the periodic 1D chain shown in Fig. 1 (a):

$$\begin{cases} m\ddot{u}_n + k\big(2u_n - u_{n-1} - u_{n+1}\big) + k_R\big(u_n - u_R\big) \\ +k_{NL}(u_n - u_{n-1})^3 + k_{NL}(u_n - u_{n+1})^3 = 0 \\ m_R\ddot{u}_R + k_R\big(u_R - u_n\big) = 0 \end{cases} \tag{A.1}$$

Subsequently, following the Lindstedt–Poincaré method [57], we consider the following asymptotic expansions:

$$\begin{aligned} u_j &= u_j^{(0)} + \epsilon\, u_j^{(1)} + O\left(\epsilon^2\right), \\ u_R &= u_R^{(0)} + \epsilon\, u_R^{(1)} + O\left(\epsilon^2\right), \\ \omega &= \omega_{(0)} + \epsilon\, \omega_{(1)} + O\left(\epsilon^2\right), \end{aligned} \tag{A.2}$$

where $j = \{n-1, n, n+1\}$. Then, we introduce (A.2) into (A.1) and obtain

$$\epsilon^0 : \begin{cases} m\omega_{(0)}^2 u_n^{(0)} + k(2u_n^{(0)} - u_{n-1}^{(0)} - u_{n+1}^{(0)}) + k_R(u_n^{(0)} - u_R^{(0)}) = 0 \\ m_R\omega_{(0)}^2 u_R^{(0)} + k_R(u_R^{(0)} - u_n^{(0)}) = 0 \end{cases} \tag{A.3}$$

$$\epsilon^1 : \begin{cases} m\omega_{(0)}^2 u_n^{(1)} + k(2u_n^{(1)} - u_{n-1}^{(1)} - u_{n+1}^{(1)}) + k_R(u_n^{(1)} - u_R^{(1)}) \\ +2m\omega_{(0)}\omega_{(1)}u_n^{(0)} + k_{NL}[(u_n^{(0)} - u_{n-1}^{(0)})^3 + (u_n^{(0)} - u_{n+1}^{(0)})^3] = 0 \\ m_R\omega_{(0)}^2 u_R^{(1)} + k_R(u_R^{(1)} - u_n^{(1)}) + 2m_R\omega_{(0)}\omega_{(1)}u_R^{(0)} = 0 \end{cases} \tag{A.4}$$

The system of equations (A.3) represents the order ϵ^0 equations, whereas (A.4) represents the order ϵ^1 equations. Subsequently, we consider the following harmonic wave solution:

$$\begin{aligned} u_j^{(0)} &= \frac{U^{(0)}}{2}\exp(ij\kappa d)\exp(i\omega t) + \frac{U^{(0)*}}{2}\exp(-ij\kappa d)\exp(-i\omega t), \\ u_R^{(0)} &= \frac{U_R^{(0)}}{2}\exp(in\kappa d)\exp(i\omega t) + \frac{U_R^{(0)*}}{2}\exp(-in\kappa d)\exp(-i\omega t), \end{aligned} \tag{A.5}$$

where * denotes the complex conjugate, and $j = \{n-1, n, n+1\}$. Then, we apply the harmonic solution to (A.4) and obtain

$$\begin{cases} m m_R \omega_{(0)}^4 u_n^{(1)} + m k_R \omega_{(0)}^2 u_n^{(1)} + k m_R \omega_{(0)}^2 (2u_n^{(1)} - u_{n-1}^{(1)} - u_{n+1}^{(1)}) \\ + m_R k_R \omega_{(0)}^2 u_n^{(1)} + k_R (2u_n^{(1)} - u_{n-1}^{(1)} - u_{n+1}^{(1)}) = \\ = C_1 \exp(i\omega_{(0)} t) \exp(in\kappa d) + C_3 \exp(3i\omega_{(0)} t) \exp(3in\kappa d) \\ m_R \omega_{(0)}^2 u_R^{(1)} + k_R (u_R^{(1)} - u_n^{(1)}) = C_{1,R} \exp(i\omega t) \exp(in\kappa d) \end{cases} \tag{A.6}$$

where the coefficients C_1 and C_3 are

$$\begin{aligned} C_1 =& (k k_R - m_R \omega_{(0)}^2 k) \Big[k k_R \, \omega_{(0)} \omega_{(1)} - \frac{3}{2} k_{NL} k_R \big(1 - \cos(\kappa d)\big)^2 \left|U^{(0)}\right|^2 \Big] U^{(0)} \\ & + m_R \, \omega_{(0)} \omega_{(1)} \frac{k_R^2}{k_R - \omega_{(0)}^2 m_R} \, U^{(0)}, \\ C_3 =& \frac{1}{2} \, \frac{k_{NL} k_R}{k} \big(k_R - 9k\omega_{(0)}^2\big) \big(2\cos^3(\kappa d) + 3\cos^2(\kappa d) - 1\big) \big(U^{(0)}\big)^2, \\ C_{1,R} =& m_R \, k_R \, \omega_{(0)} \omega_{(1)} \, \frac{1}{k_R - \omega_{(0)}^2 m_R} \, U^{(0)}. \end{aligned} \tag{A.7}$$

More precisely, we consider $U^{(0)} \, U^{(0)^*} = \left|U^{(0)}\right|^2$ in (A.7). The forcing terms on the right-hand side of the first equation in (A.6) are secular; therefore, we determine that C_1 is equal to 0. We then apply the F–B boundary conditions on the left and right-hand bounds via controlled displacements to the $(n-1)^{th}$ and $(n+1)^{th}$ masses, respectively. Consequently, we can define the analytical expression of $\omega_{(1)}$, which corresponds to $\mathbf{FRF^{(1)}}$ in the form $\frac{U}{U_{left}}$. Finally, we obtain Eq. (13), i.e.

$$\mathbf{FRF^{(1)}} = \left(\frac{2 \, m_R \, \omega_{(0)} \, \omega_{(1)} \left(k_R^2 \, m_R + m \, k_R^2 - 2 \, m \, k_R \, m_R \, \omega_{(0)}^2 + m \, m_R^2 \, \omega_{(0)}^4\right)}{3 \, k_{NL} \, m \left(k_R - m_R \, \omega_{(0)}^2\right)^2 \left[1 - \exp(2i\kappa d)\right]^2 |U_{left}|^2} \right)^{\frac{1}{2}}. \tag{A.8}$$

It is easy to verify that the linear term $\mathbf{FRF^{(0)}}$ is obtained by substituting harmonic solutions (A.5) in the form of $\frac{U^{(0)}}{U_{left}}$ into (A.3).

Appendix B. The transfer matrix method applied to the bi-material Euler–Bernoulli beam's unit cell

The transfer matrix method requires the solution of the following eigenvalue problem:

$$\bar{\mathbf{T}}_{\mathbf{q}}(\omega)\bar{\mathbf{\Gamma}}_{\mathbf{0}} = \lambda_q \bar{\mathbf{\Gamma}}_{\mathbf{0}} = \bar{\mathbf{\Gamma}}_{\mathbf{a}}, \tag{B.1}$$

$$\bar{\mathbf{T}}_{\mathbf{w}}(\omega)\bar{\mathbf{\Psi}}_{\mathbf{0}} = \lambda_a \bar{\mathbf{\Psi}}_{\mathbf{0}} = \bar{\mathbf{\Psi}}_{\mathbf{a}}, \tag{B.2}$$

where $\bar{\mathbf{T}}$ is the transfer matrix, $\lambda = \exp(i\kappa a)$ are the eigenvalues, and $\mathbf{\Gamma}$ and $\mathbf{\Psi}$ are the state vectors containing displacements and forces, for axial and flexural vibrations, respectively. $\mathbf{0}$ and $\mathbf{a}$ indicate the two ends of the unit cell, see Fig. 17. The state vectors for the axial vibrations, are defined as follows:

$$\bar{\mathbf{\Gamma}}_{\mathbf{0}} = [q(0)\ F_q(0)]^{\mathrm{T}}, \tag{B.3}$$

$$\bar{\mathbf{\Gamma}}_{\mathbf{a}} = [q(a)\ F_q(a)]^{\mathrm{T}}, \tag{B.4}$$

where T indicates the transpose. The state vectors for the flexural vibrations are defined as follows:

$$\bar{\mathbf{\Psi}}_{\mathbf{0}} = [u(0)\ \theta(0)\ V(0)\ M(0)]^{\mathrm{T}}, \tag{B.5}$$

$$\bar{\mathbf{\Psi}}_{\mathbf{a}} = [u(a)\ \theta(a)\ V(a)\ M(a)]^{\mathrm{T}}. \tag{B.6}$$

The equations are arranged by using the Euler–Bernoulli beam theory set in (32)-(37). We can arrange the equations in matrix form while ensuring continuity and force balance, since the steel and the lead are treated as different beams. Therefore, the relevant equations read:

$$\mathbf{T}_{\mathbf{q}}(\omega)\mathbf{\Gamma}_{\mathbf{0}} = \mathbf{\Gamma}_{\mathbf{a}}, \tag{B.7}$$

$$\mathbf{T}_{\mathbf{w}}(\omega)\mathbf{\Psi}_{\mathbf{0}} = \mathbf{\Psi}_{\mathbf{a}}, \tag{B.8}$$

where $\mathbf{T_q}$ is a 8x8 matrix, $\mathbf{T_w}$ is a 14x14 matrix, while $\mathbf{\Gamma}$ and $\mathbf{\Psi}$ are defined as follows:

$$\mathbf{\Gamma_0} = [q_{st}(0)\ F_{q,st}(0)\ q_{st}(l)\ F_{q,st}(l)\ q_{le}(0)\ F_{q,le}(0)\ Q_{st}\ Q_{le}]^{\mathrm{T}}, \tag{B.9}$$

$$\mathbf{\Gamma_a} = [q_{le}(a)\ F_{q,le}(a)\ \mathbf{0}_q]^{\mathrm{T}}, \tag{B.10}$$

$$\mathbf{\Psi_0} = [w_{st}(0)\ \theta_{st}(0)\ V_{st}(0)\ M_{st}(0)\ w_{st}(l)\ \theta_{st}(l)\ V_{st}(l)\ M_{st}(l)\ w_{le}(0)\ \theta_{le}(0)\ V_{le}(0)\ M_{le}(0)\ w_{st}\ w_{le}]^{\mathrm{T}}, \tag{B.11}$$

$$\mathbf{\Psi_0} = [w_{le}(l)\ \theta_{le}(l)\ V_{le}(l)\ M_{le}(l)\ \mathbf{0}_w]^{\mathrm{T}}, \tag{B.12}$$

where $\mathbf{0}_q$ and $\mathbf{0}_w$ are 1x6 and 1x10 matrices, respectively. To obtain the transfer matrices, the matrices $\mathbf{T_q}$ and $\mathbf{T_w}$ in Eq.(B.7) and Eq.(B.8) must be reduced as follows:

$$\bar{\mathbf{T}}_\mathbf{q} = \mathbf{T}_{\mathbf{q}d,d} - \mathbf{T}_{\mathbf{q}d,e}(\mathbf{T}_{\mathbf{q}e,e}^{-1}\mathbf{T}_{\mathbf{q}e,d}), \tag{B.13}$$

$$\bar{\mathbf{T}}_\mathbf{w} = \mathbf{T}_{\mathbf{w}d,d} - \mathbf{T}_{\mathbf{w}d,e}(\mathbf{T}_{\mathbf{w}e,e}^{-1}\mathbf{T}_{\mathbf{w}e,d}), \tag{B.14}$$

where d ranges from 1 to 2 and e from 3 to 12 for the axial vibrations, whereas for the flexural vibrations, d ranges from 1 to 4 and e from 5 to 22. Once the eigenvalues λ_q and λ_w have been calculated from (B.1) and (B.2) for a selected frequency ω, we can obtain the corresponding wavenumber as follows:

$$\kappa_r = \frac{1}{a}\mathrm{atan}\Big(\frac{\Im(\lambda)}{\Re(\lambda)}\Big), \tag{B.15}$$

$$\kappa_i = \frac{\ln|\lambda|}{a}. \tag{B.16}$$

References

[1] H. Zhang, J. Paik, Kirigami design and modeling for strong, lightweight metamaterials, Advanced Functional Materials 32 (21) (2022) 2107401.

[2] Y. Nian, S. Wan, M. Avcar, R. Yue, M. Li, 3d printing functionally graded metamaterial structure: Design, fabrication, reinforcement, optimization, International Journal of Mechanical Sciences 258 (2023) 108580.

[3] D. Han, X. Ren, Y. Zhang, X. Y. Zhang, X. G. Zhang, C. Luo, Y. M. Xie, Lightweight auxetic metamaterials: Design and characteristic study, Composite Structures 293 (2022) 115706.

[4] M. Mazzotti, A. Foehr, O. R. Bilal, A. Bergamini, F. Bosia, C. Daraio, N. M. Pugno,

M. Miniaci, Bio-inspired non self-similar hierarchical elastic metamaterials, International Journal of Mechanical Sciences 241 (2023) 107915.

[5] K. K. Dudek, J. A. I. Martínez, G. Ulliac, M. Kadic, Micro-scale auxetic hierarchical mechanical metamaterials for shape morphing, Advanced Materials 34 (14) (2022) 2110115.

[6] L. Van Belle, C. Claeys, E. Deckers, W. Desmet, On the impact of damping on the dispersion curves of a locally resonant metamaterial: Modelling and experimental validation, Journal of Sound and Vibration 409 (2017) 1–23.

[7] C. L. Bacquet, H. Al Ba'ba'a, M. J. Frazier, M. Nouh, M. I. Hussein, Metadamping: dissipation emergence in elastic metamaterials, Advances in applied mechanics 51 (2018) 115–164.

[8] H. Yasuda, P. R. Buskohl, A. Gillman, T. D. Murphey, S. Stepney, R. A. Vaia, J. R. Raney, Mechanical computing, Nature 598 (7879) (2021) 39–48.

[9] L. J. Kwakernaak, M. van Hecke, Counting and sequential information processing in mechanical metamaterials, Phys. Rev. Lett. 130 (2023) 268204. doi:10.1103/PhysRevLett.130.268204.

[10] Y. Zeng, L. Cao, S. Wan, T. Guo, Y.-F. Wang, Q.-J. Du, B. Assouar, Y.-S. Wang, Seismic metamaterials: Generating low-frequency bandgaps induced by inertial amplification, International Journal of Mechanical Sciences 221 (2022) 107224.

[11] A. Colombi, R. Zaccherini, G. Aguzzi, A. Palermo, E. Chatzi, Mitigation of seismic waves: Metabarriers and metafoundations bench tested, Journal of Sound and Vibration 485 (2020) 115537. doi:https://doi.org/10.1016/j.jsv.2020.115537.

[12] F. Aloschi, R. Andreotti, O. S. Bursi, Pipe vibration attenuation through internal damping and optimal design of vibro-impact systems, Scientific Reports 13 (1) (2023) 6510.

[13] N. Karathanasopoulos, F. Dos Reis, Extending the elastic and plastic design space of metamaterials through load-specific, multiscale inner material architectures, International Journal of Mechanical Sciences 175 (2020) 105523.

[14] N. Ma, Q. Han, S. Han, C. Li, Hierarchical re-entrant honeycomb metamaterial for energy absorption and vibration insulation, International Journal of Mechanical Sciences 250 (2023) 108307.

[15] A. Bayat, S. Gaitanaros, Wave directionality in three-dimensional periodic lattices, Journal of Applied Mechanics 85 (1) (2018) 011004.

[16] Z. Tao, X. Ren, L. Sun, Y. Zhang, W. Jiang, A. G. Zhao, Y. M. Xie, A novel re-entrant honeycomb metamaterial with tunable bandgap, Smart Materials and Structures 31 (9) (2022) 095024.

[17] S. Wen, Y. Xiong, S. Hao, F. Li, C. Zhang, Enhanced band-gap properties of an acoustic metamaterial beam with periodically variable cross-sections, International Journal of Mechanical Sciences 166 (2020) 105229.

[18] L. Wu, Y. Wang, K. Chuang, F. Wu, Q. Wang, W. Lin, H. Jiang, A brief review of dynamic mechanical metamaterials for mechanical energy manipulation, Materials Today 44 (2021) 168–193.

[19] L. Xiao, O. S. Bursi, H. Li, M. Wang, X.-L. Du, Energy dissipation enhancement of flexural metamaterial beams with inerter and rotational deformation, International Journal of Mechanical Sciences 237 (2023) 107770.

[20] G. Ma, P. Sheng, Acoustic metamaterials: From local resonances to broad horizons, Science advances 2 (2) (2016) e1501595.

[21] M. I. Hussein, M. J. Leamy, M. Ruzzene, Dynamics of phononic materials and structures: Historical origins, recent progress, and future outlook, Appl. Mech. Rev. 66 (4) (05 2014). doi:10.1115/1.4026911.

[22] A. Banerjee, R. Das, E. P. Calius, Waves in structured mediums or metamaterials: A review, Archives of Computational Methods in Engineering 26 (2019). doi:10.1007/s11831-018-9268-1.

[23] D. Mu, H. Shu, L. Zhao, S. An, A review of research on seismic metamaterials, Advanced Engineering Materials 22 (11) (2020) 1901148.

[24] Z. Liu, X. Zhang, Y. Mao, Y. Zhu, Z. Yang, C. T. Chan, P. Sheng, Locally resonant sonic materials, science 289 (5485) (2000) 1734–1736.

[25] L. Ribeiro, V. Dal Poggetto, B. Huallpa, J. Arruda, Bloch wavenumber identification of periodic structures using prony's method, Mechanical Systems and Signal Processing 178 (2022) 1–18. doi:https://doi.org/10.1016/j.ymssp.2022.109242.

[26] K.-C. Chuang, D.-F. Wang, X. Fang, Y.-H. Wang, Z.-L. Huang, Applying bandgap defect modes to crack detection in beams using periodic concentrated masses, Journal of Sound and Vibration 477 (2020) 115308.

[27] Y. Xu, G. Huang, Modal sensitivity analysis of acoustic metamaterials for structural damage detection, International Journal of Mechanical Sciences 259 (2023) 108571.

[28] C. He, K. M. Lim, X. Liang, F. Zhang, J. Jiang, Tunable band structures design for elastic wave transmission in tension metamaterial chain, European Journal of Mechanics-A/Solids 92 (2022) 104481.

[29] S. Lenci, E. Pavlovskaia, G. Rega, M. Wiercigroch, Rotating solutions and stability of parametric pendulum by perturbation method, Journal of Sound and Vibration 310 (2008) 243–259.

[30] M. D. Fronk, L. Fang, P. Packo, M. J. Leamy, Elastic wave propagation in weakly nonlinear media and metamaterials: a review of recent developments, Nonlinear Dynamics 111 (12) (2023) 10709–10741.

[31] B. S. Lazarov, J. S. Jensen, Low-frequency band gaps in chains with attached non-linear oscillators, International Journal of Non-Linear Mechanics 42 (10) (2007) 1186–1193.

[32] Z. Hao, Q. Cao, M. Wiercigroch, Nonlinear dynamics of the quasi-zero-stiffness sd oscillator based upon the local and global bifurcation analyses, Nonlinear dynamics 87 (2017) 987–1014.

[33] I. Antoniadis, D. Chronopoulos, V. Spitas, K. D., Hyper-damping properties of a stiff and stable linear oscillator with a negative stiffness element, Journal of Sound and Vibration 346 (2015) 37–52.

[34] M. Wenzel, O. Bursi, I. Antoniadis, Optimal finite locally resonant metafoundations enhanced with nonlinear negative stiffness elements for seismic protection of large storage tanks, Journal of Sound and Vibration 483 (2015) 115488.

[35] T. Guner, O. Bursi, S. Erlicher, Optimization and performance of metafoundations for seismic isolation of small modular reactors, Computer-Aided Civil and Infrastructure Engineering 38 (2023) 1558–1582.

[36] Y. Xia, M. Ruzzene, A. Erturk, Dramatic bandwidth enhancement in nonlinear metastructures via bistable attachments, Applied Physics Letters 114 (2019) 093501. doi:10.1063/1.5066329.

[37] B. Deng, W. P., V. Tournat, K. Bertoldi, Nonlinear transition waves in free-standing bistable chains, Journal of the Mechanics and Physics of Solids 136 (2020) 103661. doi:https://doi.org/10.1016/j.jmps.2019.07.004.

[38] T. Guner, O. Bursi, S. Broccardo, Seismic vibration mitigation of steel storage tanks by metafoundations endowed with linear and bistable columns, Bulletin of Earthquake Engineering (2023). doi:https://doi.org/10.1007/s10518-023-01692-0.

[39] M. Hussein, R. Khajehtourian, Nonlinear bloch waves and balance between hardening and softening dispersion, Proceedings of the Royal Society A: Mathematical, Physical and Engineering Sciences 474 (2217) (2018) 20180173.

[40] K. Manktelow, M. J. Leamy, M. Ruzzene, Multiple scales analysis of wave–wave interactions in a cubically nonlinear monoatomic chain, Nonlinear Dynamics 63 (2011) 193–203.

[41] M. Campana, M. Ouisse, E. Sadoulet-Reboul, M. Ruzzene, S. Neild, F. Scarpa, Impact of nonlinear resonators in periodic structures using a perturbation approach, Mechanical Systems and Signal Processing 135 (2020) 106408. doi:https://doi.org/10.1016/j.ymssp.2019.106408.

[42] X. Fang, J. Wen, B. Bonello, J. Yin, D. Yu, Wave propagation in one-dimensional nonlinear acoustic metamaterials, New Journal of Physics 19 (5) (may 2017). doi:10.1088/1367-2630/aa6d49.

[43] M. Ruzzene, F. Scarpa, F. Soranna, Wave beaming effects in two-dimensional cellular structures, Smart Materials and Structures 12 (3) (2003) 363–372. doi:10.1088/0964-1726/12/3/307.

[44] M. Collet, M. Ouisse, M. Ruzzene, M. Ichchou, Floquet–bloch decomposition for the computation of dispersion of two-dimensional periodic, damped mechanical systems, International Journal of Solids and Structures 48 (20) (2011) 2837–2848. doi:https://doi.org/10.1016/j.ijsolstr.2011.06.002.

[45] V. Settimi, M. Lepidi, A. Bacigalupo, Nonlinear dispersion properties of one-dimensional mechanical metamaterials with inertia amplification, International Journal of Mechanical Sciences 201 (2021) 106461.

[46] Y.-Z. Wang, F.-M. Li, Y.-S. Wang, Influences of active control on elastic wave propagation in a weakly nonlinear phononic crystal with a monoatomic lattice chain, International Journal of Mechanical Sciences 106 (2016) 357–362.

[47] S. Sepehri, M. M. Mashhadi, M. M. S. Fakhrabadi, Dispersion curves of electromagnetically actuated nonlinear monoatomic and mass-in-mass lattice chains, International Journal of Mechanical Sciences 214 (2022) 106896.

[48] L. Junyi, D. Balint, An inverse method to determine the dispersion curves of periodic structures based on wave superposition, Journal of Sound and Vibration 350 (Jul 2014) 41–72. doi:https://doi.org/10.1016/j.jsv.2015.03.041.

[49] P. Margerit, A. Lebée, J.-F. Caron, K. Ege, X. Boutillon, The high-resolution wavevector analysis for the characterization of the dynamic response of composite plates, Journal of Sound and Vibration 458 (2019) 177–196. doi:https://doi.org/10.1016/j.jsv.2019.06.026.

[50] J. G. McDaniel, W. S. Shepard, Estimation of structural wave numbers from spatially sparse response measurements, The Journal of the Acoustical Society of America 108 (4) (2000) 1674–1682. doi:10.1121/1.1310668.

[51] J. Berthaut, M. Ichchou, L. Jezequel, K-space identification of apparent structural behaviour, Journal of Sound and Vibration 280 (3) (2005) 1125–1131. doi:https://doi.org/10.1016/j.jsv.2004.02.044.

[52] L. Junyi, V. Ruffini, D. Balint, Measuring the band structures of periodic beams using the wave superposition method, Journal of Sound and Vibration 382 (2016) 158–178.

[53] Y. Vered, E. Baruch, I. Bucher, Experimental dispersion identification using a fitted state-space model, Journal of Sound and Vibration 517 (2022) 116580.

[54] M. I. Albakri, V. V. Sriram Malladi, S. Gugercin, P. A. Tarazaga, Estimating dispersion curves from frequency response functions via vector-fitting, Mechanical Systems and Signal Processing 140 (2020) 106597. doi:https://doi.org/10.1016/j.ymssp.2019.106597.

[55] J. Lou, X. Fang, J. Du, H. Wu, Propagation of fundamental and third harmonics along a nonlinear seismic metasurface, International Journal of Mechanical Sciences 221 (2022) 107189.

[56] K. Wang, J. Zhou, D. Xu, H. Ouyang, Lower band gaps of longitudinal wave in a one-dimensional periodic rod by exploiting geometrical nonlinearity, Mechanical Systems and Signal Processing 124 (2019) 664–678.

[57] R. K. Narisetti, M. J. Leamy, M. Ruzzene, A Perturbation Approach for Predicting Wave Propagation in One-Dimensional Nonlinear Periodic Structures, Journal of Vibration and Acoustics 132 (3) (04 2010). doi:10.1115/1.4000775.

[58] H. Li, X. Wang, J. Chen, Nonlinear electro-mechanical coupling vibration of corrugated graphene/piezoelectric laminated structures, International Journal of Mechanical Sciences 150 (2019) 705–714.

[59] X. Fang, J. Wen, J. Yin, D. Yu, Y. Xiao, Broadband and tunable one-dimensional strongly nonlinear acoustic metamaterials: Theoretical study, Phys. Rev. E 94 (2016) 052206. doi:10.1103/PhysRevE.94.052206.

[60] Y. Shen, W. Lacarbonara, Nonlinear dispersion properties of metamaterial beams hosting nonlinear resonators and stop band optimization, Mechanical Systems and Signal Processing 187 (2023) 109920.

[61] R. Zivieri, F. Garescì, B. Azzerboni, M. Chiappini, G. Finocchio, Nonlinear dispersion relation in anharmonic periodic mass spring and mass in mass systems, Journal of Sound and Vibration (2019). doi:10.1016/j.jsv.2019.114929.

[62] D. Mead, Wave propagation in continuous periodic structures: research contributions from southampton, 1964-1995, Journal of Sound and Vibration 190 (3) (1996) 495–524.

[63] D. W. Marquardt, An algorithm for least-squares estimation of nonlinear parameters, Journal of the society for Industrial and Applied Mathematics 11 (2) (1963) 431–441.

[64] J. J. Moré, The Levenberg - Marquardt algorithm: Implementation and theory, In: Watson G.A. (eds) Numerical Analysis. Lecture Notes in Mathematics, vol 630 (1978). doi:https://doi.org/10.1007/BFb0067700.

[65] W. Jiao, S. Gonella, Doubly nonlinear waveguides with self-switching functionality selection capabilities, Physical Review E 99 (4) (2019) 042206.

[66] J. Liu, K. Bertoldi, Bloch wave approach for the analysis of sequential bifurcations in bilayer structures, Proceedings of the Royal Society A: Mathematical, Physical and Engineering Sciences 471 (2182) (2015) 20150493. doi:10.1098/rspa.2015.0493.

[67] A. Palermo, B. Yousefzadeh, C. Daraio, A. Marzani, Rayleigh wave propagation in nonlinear metasurfaces, Journal of Sound and Vibration 520 (2022) 116599.

[68] P. Van Overschee, B. De Moor, Two subspace algorithms for the identification of combined deterministic-stochastic systems, in: [1992] Proceedings of the 31st IEEE Conference on Decision and Control, IEEE, 1992, pp. 511–516.

[69] P. Van Overschee, B. De Moor, Subspace algorithms for the stochastic identification problem, Automatica 29 (3) (1993) 649–660.

[70] P. Van Overschee, B. De Moor, A unifying theorem for three subspace system identification algorithms, Automatica 31 (12) (1995) 1853–1864.

[71] S. Marchesiello, L. Garibaldi, A time domain approach for identifying nonlinear vibrating structures by subspace methods, Mechanical Systems and Signal Processing 22 (1) (2008) 81–101. doi:https://doi.org/10.1016/j.ymssp.2007.04.002.

[72] S. Marchesiello, E. Gandino, Identification of a Duffing oscillator under different types of excitation, Mathematical Problems in Engineering (2010). doi:https://doi.org/10.1155/2010/695025.

[73] Y. Guo, Identification of nonlinear systems with non-persistent excitation using an iterative forward orthogonal least squares regression algorithm, International Journal of Modelling Identification and Control 23 (05 2014). doi:10.1504/IJMIC.2015.067496.

[74] A. Banerjee, Non-dimensional analysis of the elastic beam having periodic linear spring mass resonators, Meccanica 55 (5) (2020) 1181–1191.

[75] S. R. Patro, A. Banerjee, G. Ramana, Vibration attenuation characteristics of finite locally resonant meta beam: Theory and experiments, Engineering Structures 278 (2023) 115506.

[76] D. Mu, K. Wang, H. Shu, J. Lu, Metamaterial beams with graded two-stage inertial amplification and elastic foundation, International Journal of Mechanical Sciences 236 (2022) 107761.

[77] J.-S. Chen, Y.-J. Huang, I.-T. Chien, Flexural wave propagation in metamaterial beams containing membrane-mass structures, International Journal of Mechanical Sciences 131 (2017) 500–506.

[78] W. Zhou, C. Lim, et al., Topological edge modeling and localization of protected interface modes in 1d phononic crystals for longitudinal and bending elastic waves, International Journal of Mechanical Sciences 159 (2019) 359–372.

[79] M. Collet, K. A. Cunefare, M. Ichchou, Wave motion optimization in periodically distributed shunted piezocomposite beam structures, Journal of Intelligent Material Systems and Structures 20 (7) (2009) 787–808.

[80] A. Singh, K. J. Moore, Identification of multiple local nonlinear attachments using a single measurement case, Journal of Sound and Vibration 513 (2021) 116410. doi:https://doi.org/10.1016/j.jsv.2021.116410.